Urban-to-downwind variations in aerosol composition and optical properties in the Paris urban plume from coordinated airborne and ground-based observations

Chenjie Yu[1], Ludovico Di Antonio[2,a], Peter F. DeCarlo[3], Benjamin A. Nault[3,4], Alejandra Velazquez-Garcia[5], Eleonora Aruffo[6,7], Piero Di Carlo[7,8], Cyrielle Denjean[5], Sarah Tinorua[5,b], Thierry Bourrianne[5], Diana L. Pereira[1,c], Kevin Tu[2,d], Edouard Pangui[2], Mathieu Cazaunau[2], Astrid Bauville[2,e], Noël Grand[1], Antonin Bergé[2,f], Claudia Di Biagio[1], Aline Gratien[1], Matthias Beekmann[1], Guillaume Siour[2], Gilles Foret[2], Barbara D'Anna[9], Julien Kammer[9], Huihui Wu[1,10], Christopher Cantrell[2], Paola Formenti[1], and Vincent Michoud[1]

[1]Université Paris Cité and Univ Paris Est Créteil, CNRS, LISA, F-75013 Paris, France
[2]Univ Paris Est Créteil and Université Paris Cité, CNRS, LISA, 94010 Créteil, France
[3]Department of Environmental Health and Engineering, Whiting School of Engineering, Johns Hopkins University, Baltimore, Maryland, USA
[4]Center for Aerosol Cloud and Chemistry, Aerodyne Research, Inc., Billerica, Massachusetts, USA
[5]Météo France, CNRS, Univ. Toulouse, CNRM, Toulouse, France
[6]Department of Science, University "G.d'Annunzio" of ChietiPescara, Chieti 66100, Italy
[7]Center for Advanced Studies and Technology (CAST), Chieti 66100, Italy
[8]Department of Advanced Technologies in Medicine & Dentistry, University "G.d'Annunzio" of ChietiPescara, Chieti 66100, Italy
[9]Aix Marseille Univ, CNRS, LCE, Marseille, France
[10]Department of Earth and Environmental Sciences, University of Manchester, Manchester M13 9PL, United Kingdom
[a]Now at: LATMOS/IPSL, Sorbonne Université, UVSQ, CNRS, 75252 Paris, France
[b]Now at: PSI Center for Energy and Environmental Sciences, 5232 Villigen PSI, Switzerland
[c]Now at: Institute for Atmospheric and Earth System Research/Physics, Faculty of Science, University of Helsinki, Helsinki, Finland
[d]Now at: Safran Aircraft Engines/Akkodis, 77550 Moissy-Cramayel, France
[e]Now at: Muséum national d'Histoire naturelle (MNHN, CNRS), BioArch, Paris, France
[f]Now at: Laboratoire des Sciences du Climat et de l'Environnement, CEA–CNRS–UVSQ, IPSL, Université Paris-Saclay, 91191 Gif-sur-Yvette, France

Correspondence to: Chenjie Yu (chenjie.yu@lisa.ipsl.fr) and Paola Formenti (paola.formenti@lisa.ipsl.fr)

Abstract.

Aerosols play a critical role in Earth's climate, yet changes in their physicochemical properties during atmospheric transport remain an important source of uncertainty in predicting their climate impacts. Observational constraints on these changes over the first few hours of urban plume transport remain limited. Here, we investigated urban-to-downwind variations in aerosol physicochemical and optical properties using coordinated ground-based and airborne measurements in Paris and its downwind region, covering estimated plume transport times of ~2–6 h. Urban plumes contributed modestly to downwind particle number concentrations in the 80–200 nm range and moderately enhanced submicron particulate matter (PM_1) relative to the surrounding background. Organic aerosol (Org) dominated PM_1 mass at both the urban site and downwind. Non-refractory

PM_1 component mass fractions and secondary aerosol mass relative to CO showed limited urban-to-downwind variations, whereas the relative contribution of more oxidized Org increased downwind. In contrast, optical properties exhibited pronounced differences, with higher plume-average single-scattering albedo at both 450 and 630 nm downwind. The complex refractive index shifted from lower real (~1.35–1.40) and higher imaginary (~0.03–0.08) components near the urban source to higher real (~1.45–1.50) and lower imaginary (~0.015–0.02) components downwind. The average absorption Ångström exponent was also higher downwind, indicating stronger wavelength dependence of aerosol absorption. These observations reveal systematic urban-to-downwind differences in aerosol physicochemical and optical properties consistent with atmospheric processing during transport. They highlight the importance of accounting for spatially evolving aerosol properties in atmospheric models and remote-sensing retrievals.

1. Introduction

Atmospheric aerosols play an important role in regulating climate through their interactions with radiation and clouds (Farmer et al., 2015; Ravishankara et al., 2015). Atmospheric aerosols also degrade air quality by impairing visibility, posing risks to human health, particularly the respiratory system, and exerting adverse impacts on natural ecosystems (Manisalidis et al., 2020). Urban areas are major sources of anthropogenic emissions and contribute substantially to aerosol burdens through activities such as transportation, industrial processes, and residential energy use (Karagulian et al., 2015). Previous studies have shown that organic aerosol (OA) constitutes a substantial fraction of total submicron particulate matter in urban environments worldwide (Zhang et al., 2007; Jimenez et al., 2009; Nault et al., 2021), with nitrate also making an important contribution compared to remote regions (Li et al., 2018). The chemical composition of urban aerosols and their associated physicochemical properties evolve continuously after emission during atmospheric aging. These aging processes, including coagulation, secondary species formation, and heterogeneous reactions, can substantially alter aerosol composition, size distribution, mixing state, optical properties, and cloud condensation nuclei (CCN) activity, thereby influencing their impacts on air quality and climate (Zaveri et al., 2010; Riemer et al., 2019).

Observational studies are essential for characterizing the evolution of urban aerosol physicochemical properties. Ground-based observations provide important insights into the temporal variability of aerosol physicochemical properties at fixed locations. Previous measurements at urban sites show that secondary organic aerosol (SOA) constitutes a substantial fraction of the organic aerosol (OA) budget in the urban environments (Chen et al., 2022), and that its rapid formation is predominantly driven by photochemical processes (Hayes et al., 2013). However, ground-based observations often represent a mixture of fresh and aged aerosols and therefore have limited ability to isolate the aerosol aging process within urban plumes. Airborne measurements offer a unique capability to directly sample urban plumes at different distances from their emission sources, enabling the investigation of aerosol evolution as a function of transport time and atmospheric processing (Kahn et al., 2023).

Airborne observations over the megacities around the world (Freney et al., 2014; Nault et al., 2018; DeCarlo et al., 2010; Schroder et al., 2018) have revealed a rapid transformation of urban aerosol compositions during the plume aging in both summer and winter. Specifically, within a few hours downwind of urban plumes, the fraction of primary organic aerosol (hydrocarbon-like organic aerosol) decreases in total PM_1 organic matter, while the fraction of secondary organic aerosol (oxygenated organic aerosol) increases correspondingly. Furthermore, Shilling et al. (2018) reported that even in environments with strong regional background SOA contributions, rapid SOA formation is still observed within a few hours of transport downwind of urban plumes.

Such efficient compositional changes within urban plumes are closely linked to the evolution of aerosol climate-relevant properties. Zaveri et al. (2022) demonstrates that the rapid SOA formation during urban plume aging in the Amazon region plays an important role in particle growth and CCN formation. Mcmeeking et al. (2012) reported an increase in the single-scattering albedo (SSA) at 550 nm downwind of the London urban plume, which is attributed to the increasing formation of secondary, non-light-absorbing aerosol components during plume aging. Dingle et al. (2016) observed enhanced aerosol extinction coefficients at 632 nm within aged urban plumes compared with fresh plumes, associated with the SOA formation during the plume aging. These changes in aerosol optical properties are fundamentally governed by the complex refractive index (CRI), which links aerosol chemical composition and mixing state to its optical behaviour and ultimately to radiative effects. As secondary aerosol formation modifies the relative contributions of scattering and absorbing components, it alters both the real and imaginary parts of the CRI, thereby influencing aerosol extinction and absorption (Wu et al., 2021; He et al., 2021). Despite its central role, observational constraints on the evolution of aerosol chemical composition and effective CRI after emission from urban regions remain limited. Chemical transport models often misrepresent aerosol chemical compositions near and downwind of anthropogenic source regions (Tsigaridis et al., 2014; Zhang et al., 2015; Jathar et al., 2017). Consequently, substantial uncertainties remain in simulating the evolution of aerosol optical properties, as models typically rely on prescribed CRI values for individual aerosol components and simplified mixing-state assumptions, which may not adequately capture their dynamic evolution during aerosol aging (Tsigaridis and Kanakidou, 2018; Brown et al., 2021). In addition, many aerosol remote sensing retrieval methods employ simplified aerosol models with prescribed optical properties (e.g. Grzegorski et al. (2022); Zhang et al. (2025)) or predefined optical properties for each aerosol component (e.g. Li et al. (2022b)). As a result, deviations between these assumptions and the actual evolution of aerosol optical properties may introduce uncertainties in retrieved aerosol optical depth (AOD), SSA, and aerosol type classification. In this context, in-situ observations of aerosol CRI provide valuable constraints for evaluating these assumptions and improving the representation of aerosol optical properties in both satellite retrieval algorithms and atmospheric models.

The Greater Paris region (Île-de-France) is a densely populated European megacity with substantial anthropogenic emissions, where aerosols play an important role in regional climate impacts and air quality according to the previous experiments (Beekmann et al., 2015). Characterizing the evolution of aerosol physicochemical properties within urban plumes is therefore

essential for understanding the relative contributions of primary emissions and secondary formation, as well as their impacts on climate-relevant properties. Previous airborne measurement (Freney et al., 2014) shows that the Paris urban plume is mainly composed of OA, BC, and particulate nitrate (pNO_3), and SOA formation is largely driven by anthropogenic gas-phase precursors. However, the impacts of the evolution of aerosol chemical components on aerosol optical properties within Paris urban plume are not addressed. Moreover, these airborne measurements were conducted more than a decade ago. In recent years, ozone (O_3) has become a prominent pollutant in many European urban environments. Declining nitrogen oxide (NO_x) emissions have been linked to rising urban O_3 levels (Grange et al., 2021), suggesting changes in atmospheric oxidative capacity and underscoring the need to re-examine the evolution of aerosol physicochemical properties during transport under current chemical conditions.

In this study, we focus on characterising urban-to-downwind variations in aerosol chemical composition and optical properties within the Paris urban plume by combining airborne and ground-based observations. Aircraft measurements conducted within the boundary layer were used to characterise the urban plume at downwind locations corresponding to estimated transport times of a few hours, providing direct observations of aerosol physicochemical properties under downwind conditions. Concurrent ground-based measurements in central Paris were used to characterise urban aerosol properties and provide an urban reference for qualitative comparison with the airborne observations. Together, these measurements provide insights into changes in aerosol optical properties from urban to downwind conditions around a major European megacity and their relationships with aerosol chemical composition, with implications for understanding the air-quality and climate effects of urban aerosols.

2. Experiment Methods and data analysis

2.1 Atmospheric Chemistry of the Suburban Forest (ACROSS) project

This study focuses on measurements obtained from aircraft observations and a ground-based site within the Atmospheric Chemistry of the Suburban Forest (ACROSS) project which provided with a broad range of observations of gas- and aerosol-phase species over the Greater Paris region (Cantrell and Michoud, 2022). A summary of the instruments used in this study and their availability together with their measurement frequencies is provided in Table S1 and Table S2 in the Supplementary Information. To enable comparison between aircraft observations and ground-based measurements, all results were reported under standard temperature and pressure (STP) conditions (T = 273.15 K, P = 1013.25 hPa) in this study.

The French environmental research aircraft SAFIRE (Service des Avions Français Instruments pour la Recherche en Environnement) ATR-42 was used to sample the evolution of Paris urban plume as part of the ACROSS project. The aircraft conducted zigzag transects across the Paris urban plume within the boundary layer at ~300–400 m above ground level (a.g.l.).

The airborne measurement was performed between 13th June and 7th July, 2022 and the flight paths are presented in Figure 1. In this study, a total of 8 flights is selected based on the availability and operational status of the instruments.

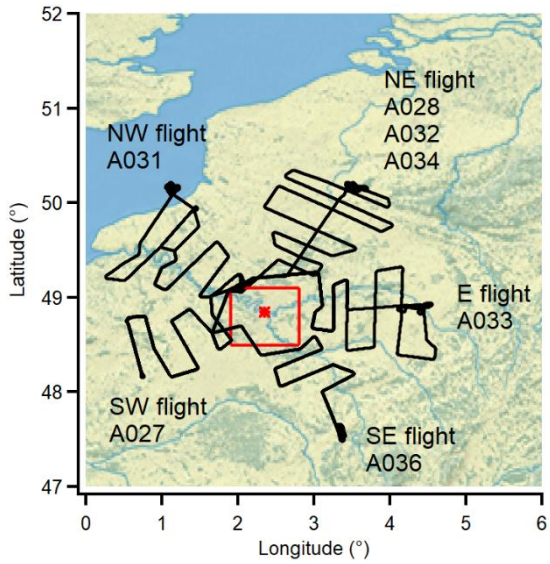

Figure 1. Flight paths of the selected ACROSS flights during the campaign. The red marker indicates the PRG site in central Paris, and the red square outlines the Greater Paris region (Île-de-France). The ATR-42 departed from Cergy Airport, located in the northwestern Greater Paris region, and conducted zigzag flight transects across the Paris urban plume. Maps were created from public domain GIS data on Natural Earth (http://www.naturalearthdata.com, last access: 01/04/2026).

The ground-based site used in this study is the Paris Rive Gauche (PRG) site (48.83° N, 2.38° E), located at Université Paris Cité in the central part of the Greater Paris Region (Di Antonio et al., 2025). The PRG measurement site was located a few hundred meters from major traffic emission sources, including train stations and urban highways. The measurements were conducted on the roof of the university building at approximately 30 m a.g.l. In this study, observations at PRG were used as an urban background reference for comparison with the Paris urban plume sampled downwind by the aircraft, rather than to represent the spatial variability of emissions across the entire metropolitan area. The periods selected from the PRG measurements for comparison with the airborne observations were determined using back-trajectory analysis, as described in Section 2.5.

2.2 SAFIRE aircraft instrumentations

2.2.1 Airborne particulate-phase measurements

A mini-Aerosol Mass Spectrometer (mAMS, Aerodyne Research, Inc.) was used to characterise the non-refractory submicron Particulate Matter (NR-PM_1) compositions and mass concentrations, including OA, sulfate (SO_4), pNO_3, ammonium (NH_4), and chloride (Chl). Note, charges are not included for the inorganic aerosol as the evaporation and fragmentation of the aerosol

leads to observing both organic and inorganic species within the SO_4, pNO_3, NH_4, and Chl family (Chen et al., 2019; Farmer et al., 2010). The mAMS has been successfully deployed in mobile ground-based (Goetz et al., 2018; Goetz et al., 2022; Werden et al., 2023) and airborne measurements (Vu et al., 2016; Konwar et al., 2024). Briefly, the mAMS is a miniaturized version of the standard compact Time-of-Flight AMS (c-ToF-AMS, Aerodyne Research, Inc.) (Drewnick et al., 2005), while maintaining comparable analytical performance. Key modifications of the mAMS compared to the standard c-ToF-AMS include a smaller vacuum chamber, and the integration of a single split-flow turbo molecular pump from the ToF Aerosol Chemical Speciation Monitor (ToF-ACSM, Aerodyne Research, Inc.) (Fröhlich et al., 2013). The mAMS measures NR-PM_1 compositions by focusing particles into a narrow beam with a critical orifice and aerodynamic lens. When particles impact on a heated metallic surface (~ 600°C), the NR-PM_1 components are vaporized, subsequently ionized by 70 eV electron impact, and quantitatively detected by ToF-MS under high vacuum. The Ionization Efficiency (IE) of the mAMS was calibrated using mono-disperse, nebulized ammonium nitrate particles at 300 nm. Default Relative Ionization Efficiency (RIE) was applied for each compound, and a constant Collection Efficiency (CE) 0.5 was applied to the final ambient results. To meet the short intercept time of Paris urban plume, the mAMS was operated in Fast mass spectrum (FMS) mode with 1 s frequency. The final results were averaged to 15s to improve the signal-to-noise ratio. The total volume of NR-PM_1 estimated from mAMS, assuming densities of 1.27 g cm^{-3} for Org and 1.77 g cm^{-3} for inorganics (Cross et al., 2007), was comparable to that derived from the particle size distribution instrument. The comparison is presented in Figure S1 in the Supplementary Information, showing a slope of 0.75 and a coefficient of determination (R^2) of 0.82. The strong correlation indicates consistent variability between the two independent measurements. The slope below unity is expected because the AMS-derived volume represents only NR-PM_1, whereas the volume derived from the UHSAS number size distribution may also include refractory aerosol components that are not detected by the AMS. Additional uncertainties associated with the assumed aerosol densities may also contribute to the difference.

The refractory black carbon (rBC)-containing particles were characterized by a Single Particle Soot Photometer (SP2, DMT). The term rBC defined here is following the definition in Petzold et al. (2013). Briefly, the SP2 employs a 1064 nm Nd:YAG crystal laser and a set of optical detectors, including scattering detectors and incandescence detectors. When an rBC-containing particle passes through the laser beam, it absorbs laser energy and becomes heated to incandescence, emitting thermal radiation in the visible to near-infrared range. The incandescence detectors then capture this signal and unambiguously identify the particle as rBC. The SP2 detects rBC components with an equivalent spherical diameter in the range of 90-700 nm. The SP2 was calibrated with mono-disperse, nebulized standard soot particles (Alfa Aesar, lot no. FS12S011) to establish the calibration ratio between particle mass concentrations and the strength of the instrument signal, and a density of 1.8 g cm^{-3} was applied to rBC (Taylor et al., 2015). SP2 data were processed using the SP2Py-Pro toolkit (Tinorua et al., 2024a; Velazquez-Garcia et al., 2026a)

The aerosol extinction and scattering coefficients at 450 nm ($\sigma_{\mathrm{ext,450\,nm}}$ and $\sigma_{scat,450\,\mathrm{nm}}$, respectively, units of $\mathrm{Mm^{-1}} = 10^{-6}$ $\mathrm{m^{-1}}$) and 630 nm ($\sigma_{\mathrm{ext,630\,nm}}$ and $\sigma_{scat,630\,\mathrm{nm}}$, respectively) were measured through the A2S2 (Aerosol Absorption Spectral Sizer, custom built), a custom-built airborne dual-wavelength cavity-attenuated phase shift single-scattering albedo monitor (CAPS-$\mathrm{PM_{SSA}}$, Aerodyne Research, Inc.) developed at LISA (CNRS), as described in detail by Yu et al. (2024). The design of the CAPS-$\mathrm{PM_{SSA}}$ is described in Onasch et al. (2015). Briefly, the instrument uses a high-reflectivity optical cavity (~99.99%) with an LED light source (450 and 630 nm for A2S2 used in this study), where σ_{ext} is derived from the phase shift change of a square-wave modulated beam when particles are present relative to a particle-free baseline. σ_{scat} is measured with an integrated sphere coated with highly reflective material acting as a nephelometer, with scattered light detected by a photomultiplier tube (PMT) to maximize light collection and minimize truncation biases. The absorption coefficient (σ_{abs}) is derived from the Extinction-Minus-Scattering (EMS) method (Weber et al., 2022). Based on laboratory intercomparison experiments (Yu et al., 2024), the measurement uncertainties in the A2S2 absorption coefficients were estimated to be 2% at 450 nm and 7% at 630 nm, respectively. The uncertainty in the Absorption Ångström exponent (AAE) derived from the A2S2 absorption coefficients at 450 and 630 nm was estimated to be approximately 20% based on comparison with the AE33. Prior to the flight campaign, the A2S2 scattering channels were calibrated using aerosolised 200 nm polystyrene latex (PSL) particles (Single Scattering Albedo (SSA) = 1), in accordance with the CAPS-$\mathrm{PM_{SSA}}$ calibration protocol. Both $\sigma_{scat,450\,\mathrm{nm}}$ and $\sigma_{scat,630\,\mathrm{nm}}$ were corrected for angular truncation using a wavelength-dependent correction based on the Scattering Ångström exponent (SAE), following the method described by Yu et al. (2024).

An Ultra-High Sensitivity Aerosol Spectrometer (UHSAS) was used to derive the particle size distribution between 40 – 1000 nm. However, considering the elevated uncertainty in the smallest UHSAS size channels near the detection limit, the first bins were excluded and only the 80 – 1000 nm size range was analysed. The coarse mode particle size distributions (~0.08 – ~10 µm) were obtained through an Optical Particle Counter (Sky-OPC, GRIMM Inc, model 1.129). The combined size distribution was constructed by merging the UHSAS and Sky-OPC datasets, with the transition between instruments defined at 1 µm. UHSAS and Sky-OPC optical diameters were converted to equivalent geometric diameters assuming the CRI of polystyrene latex (PSL; CRI = 1.59) at the instrument operating wavelengths (1054 nm for the UHSAS and 655 nm for the Sky-OPC), respectively. Cloud droplet size distributions between 2 and 50 µm were measured using a Cloud Droplet Probe (CDP, DMT). The CDP results were used to identify in-cloud periods, defined as periods when the liquid water content (LWC) exceeded 0.01 g $\mathrm{m^{-3}}$. The LWC was calculated from the droplet size distributions assuming a liquid water density of 1 g $\mathrm{cm^{-3}}$. All data corresponding to in-cloud conditions were excluded from the analysis.

Onboard the aircraft, the Sky-OPC, A2S2 and SP2 were connected to the AVIRAD measurement system, consisting an isoaxial and isokinetic inlet located below the aircraft and characterised by a collection efficiency of 50% at 12 µm in particle optical diameter (Formenti et al., 2011). The mAMS was connected to a Rosemount inlet mounted on the side of the fuselage via a

stainless-steel sampling line, providing near-unity transmission efficiency for submicron particles (Capes et al., 2008). The stainless-steel sampling line between the mAMS and the Rosemount inlet was ~1 m, corresponding to an estimated residence time of ~0.6 s, and the influence of residence time on the measured aerosol composition is expected to be negligible. Although no dryer was used upstream of these instruments onboard the aircraft, the RH measured at the inlet remained below 40% during the selected airborne measurement periods due to ram heating (presented in Table S6 in the Supplementary Information). Thus, the measurements were considered to represent near-dry aerosol conditions.

2.2.2 Airborne gas-phase measurements

NO_2 measurements were conducted using a four-channel Thermal Dissociation Laser Induced Fluorescence (TD-LIF). Details of the TD-LIF principles and its airborne deployment are provided in Di Carlo et al. (2013). The instrument detects NO_2 via laser-induced fluorescence following excitation at 532 nm, while additional total gas-phase nitrogen species (NO_y) species are quantified through controlled thermal dissociation in parallel heated channels. To distinguish these gas-phase reactive nitrogen measurements from particulate nitrate measured by the mAMS/ACSM, the latter is denoted as pNO_3 throughout this study. Total Peroxy Nitrates (ΣPNs), total Alkyl Nitrates (ΣANs), and nitric acid (HNO_3) are thermally decomposed into NO_2 at approximately 200°C, 350°C, and 600°C, respectively, with the resulting NO_2 subsequently measured by LIF. The TD-LIF was calibrated using standard cylinder of NO_2 and zero air. However, TD-LIF measurements were not available during Flight A036, and NO_2 was instead measured using a CAPS-NO_2 instrument (Teledyne, T500U). The CAPS-NO_2 was calibrated before and after the campaign using the same procedure as for the TD-LIF instrument. Owing to the faster response time and lower detection limit of TD-LIF compared to CAPS-NO_2 (as described in Table S1 in the Supplementary Information), absolute NO_2 concentrations reported in this study were based on TD-LIF measurements. The CAPS-NO_2 data for Flight A036 were used only in a relative sense to identify plume periods, and the corresponding absolute NO_2 concentrations were not included in the final analysis. O_3 was measured through an ozone analyser (Thermo Scientific, Model 49i), and CO was measured through an in-flight gas concentration analyser (PICARRO, G2401-m).

The regional background concentrations of CO, NO_2, and rBC were defined as the 5th percentile of the measurements from each flight and were used for plume identification. Background concentrations of aerosol and gas-phase species were determined from the nearest out-plume measurements, as shown in Figure 2(a).

2.2.3 Airborne meteorological parameter measurements

The air temperature and relative humidity (RH) were measured through a Rosemount housing (E102AL Rosemount) and a 1011C hygrometer onboard the aircraft, respectively. Horizontal wind speed and direction were derived from a combination of airspeed and flow angle measurements from a nose-mounted gust probe and aircraft motion data from the onboard inertial

navigation system (INS)/GPS. The results of average meteorological parameters for each flight are presented in Table S6 in the Supplementary Information.

2.3 Ground based measurements in Paris urban site

At PRG ground-based site, a ToF-ACSM was used to characterise the NR-PM_1 compositions. The ACSM measures the chemical composition of NR-PM_1 using principles similar to those of the mAMS, including aerodynamic focusing, thermal vaporization, and electron-impact ionization. Ammonium nitrate and ammonium sulfate was used to do the calibrations. The IE of ACSM has also been calibrated using mono-disperse, nebulized ammonium nitrate particles at 300 nm. The RIE of NH_4 and SO_4 for the ACSM were determined from measurements of 300 nm ammonium nitrate and ammonium sulfate particles, respectively. A constant CE 0.5 was applied to the final ambient results. It should be noted that signals at specific mass-to-charge (m/z) ratios derived from mAMS and ACSM measurements are not strictly comparable, as differences in instrument design and operating principles (e.g., vaporization and sampling protocols) can introduce systematic variations in the measured signals (Pieber et al., 2016). Therefore, detailed comparisons of individual m/z signals (e.g., m/z 44 and 43) between mAMS and ACSM were not considered in this study.

The σ_{scat} of PM_1 particles at 450, 550 and 700 nm was measured through a Nephelometer (NEPH, Ecotech Aurora 4000), while the σ_{abs} of PM_1 at seven different wavelengths (370, 470, 520, 590, 660, and 880 and 950 nm) was measured by a dual-spot aethalometer (AE33, Magee Sci.) (Yus-Díez et al., 2021). Details of the PRG optical instrumentation and data analysis are described in Di Antonio et al. (2025). NEPH measures the aerosol scattering coefficient by illuminating an aerosol sample with a collimated light source and detecting the light scattered by particles over a range of angles $(9-170^{\circ})$ using photodetectors. Correction of the NEPH truncation error was performed according to the submicron aerosol formulation described by Teri et al. (2022). The AE33 measures the light attenuation coefficient (σ_{atn}) through a filter tape, which was sampled at 1-minute intervals. The spectral aerosol absorption coefficient is determined as:

$$\boldsymbol{\sigma_{\mathrm{abs}}} = \frac{\boldsymbol{\sigma_{\mathrm{atn}}}}{\boldsymbol{C_{\mathrm{ref}}}} \qquad (1)$$

Where C_{ref} is the multiple scattering correction factor. While the filter-based AE33 quantifies σ_{abs} via transmittance attenuation from deposited particles, its accuracy is compromised by multi-scattering interactions within the filter matrix, including variable aerosol loading and filter leakage. A wavelength-independent C_{ref} of 2.45 has been applied to correct the final absorption coefficient results as recommended by ACTRIS (Savadkoohi et al., 2023). The light absorbing equivalent Black Carbon (eBC) mass concentration is derived from the multiple scattering corrected 880 nm channel results using a mass absorption cross section (MAC) of 7.77 $m^2\ g^{-1}$ (Petzold et al., 2013; Bond et al., 2013). As BC was characterized using different definitions, reported as eBC by the AE33 at PRG and as rBC by the SP2 onboard the aircraft, their absolute mass concentrations are not directly comparable. A simplified factor of 2 was applied to convert the AE33-derived eBC mass concentrations to rBC-equivalent mass concentrations, based on previous AE33–SP2 intercomparisons (Laing et al., 2020; Tinorua et al., 2024b).

These studies reported AE33-derived eBC concentrations approximately twice the SP2-measured rBC concentrations when using the manufacturer-recommended multiple-scattering correction for AE33. In this study, a higher wavelength-independent multiple-scattering correction factor (2.14) was applied, resulting in lower derived eBC mass concentrations and thus applying a conversation factor of 2 likely providing a conservative estimate of the rBC-equivalent mass concentration when applying the same conversion factor. The converted AE33-derived rBC-equivalent mass concentration results were only used to illustrate the relative changes in the rBC mass fraction (presented in Figure S2 in the Supplementary Information). The σ_{scat} measured by NEPH and the σ_{abs} measured by AE33 have been scaled to match the airborne A2S2 wavelengths, as described in Section 2.4. The σ_{ext} of PM_1 at 450 and 630 nm was then calculated as the sum of σ_{scat} and σ_{abs} at the corresponding wavelengths. Yu et al. (2024) has demonstrated that the σ_{scat}, σ_{abs} and σ_{ext} at 450 and 630 nm derived from A2S2 agree well with measurements from the NEPH and AE33, respectively, across a range of aerosol loading conditions. Weber et al. (2022) similarly demonstrated that CAPS-PM_{SSA} measurements are comparable to those from NEPH and other optical instruments at these wavelengths. These findings support the intercomparison of airborne and PRG optical properties in this study.

The particles size distribution at PRG was measured through a Scanning Mobility Particle Sizer (SMPS) which consists of a Differential Mobility Analyzer (DMA, TSI model 3082) and a Condensation Particle Counter (CPC, TSI model 3776). Sheath and aerosol flow were fixed at 3.0 L min^{-1} and 0.3 L min^{-1}, to measure particle size distribution across 23-982 nm range, with one scan measured every 2 minutes. The SMPS mobility diameters were interpreted as equivalent geometric diameters by assuming spherical particles with a shape factor of 1.

All aerosol measurement instruments (ACSM, SMPS, AE33, and NEPH) were connected to a PM_1 sampling head. A Nafion dryer was applied before the ACSM. Air was drawn through a 10 m copper tube from the PM_1 inlet to a four-way stainless-steel flow splitter (TSI) located in the measurement room, which distributed the airflow to the individual instruments. Losses by diffusion were calculated individually for each instrument using the Particle Loss Calculator (PLC; developed by the Max Planck Institute (Von Der Weiden et al., 2009)) as a function of the sampling-line geometry (e.g., curvature and tube dimensions) and aerosol properties (Baron and Willeke, 2001). The calculated losses were used to assess the performance of the modified inlet system and were not applied to correct the measured aerosol properties, as the estimated losses were generally below 10% over the particle size range considered.

NO_2 was measured by an ozone chemiluminescence analyzer (model AC32M, Envea), and O_3 was measured through a UV-absorption monitor (model O3-41M, Envea). More details of the gas-phase measurements at PRG are described in Pereira et al. (2025). The CO data were taken from the closest AIRPARIF (Association Interdépartementale pour la gestion du Réseau automatique de surveillance de la Pollution Atmosphérique et d'Alerte en Région d'Île-de-France) monitoring site, situated in central Paris (Châtelet–Les Halles), at a distance of ~6 km from the PRG site location. The background CO concentration at PRG for each flight period was defined using the average out-plume CO concentration measured closer to the city during the

corresponding flight, as these measurements were conducted within the boundary layer and were considered representative of the near-surface background surrounding the urban plume. As a sensitivity test, the analysis was repeated using the 5th percentile of the daily PRG measurements as the PRG background, with the corresponding results presented in the Supplementary Information (Figure S4). Although the absolute values changed with the choice of background, the overall patterns of variation between the PRG and downwind measurements remained.

2.4 Optical properties evaluation and derivation of the dry aerosol complex refractive index (CRI)

For comparisons at the consistent wavelengths with the airborne A2S2 wavelengths, the PRG NEPH and AE33 results have been scaled using the Ångström exponent approach using equation (3):

$$\boldsymbol{xAE} = -\frac{\ln(\sigma_{\lambda_1}/\sigma_{\lambda_2})}{\ln(\lambda_1/\lambda_2)} \quad (2)$$

Where xAE is the Scattering or Absorption Ångström Exponent (SAE, AAE), σ_{λ_1} and σ_{λ_2} represent the scattering or absorption coefficient at wavelengths λ_1 and λ_2 respectively. The absorption or the scattering coefficient (σ_λ) at a given wavelength (λ, 450 or 630 nm) can be derived through equation (4):

$$\boldsymbol{\sigma_\lambda} = \boldsymbol{\sigma_{\lambda_0}} \cdot \left(\frac{\lambda}{\lambda_0}\right)^{-x\mathbf{AE}} \quad (3)$$

Where σ_{λ_0} is the absorption or scattering coefficient at the wavelength λ_0. In this study, the σ_{sca} at 630 nm for the NEPH is derived through measurements at 700 nm, and the σ_{abs} at 450 and 630 nm for the AE33 is derived through absorption measurements at 470 and 660 nm, respectively.

The BrC absorption coefficient is determined in the assumption that absorption at 630 nm is contributed by BC only and the AAE for BC is 1. Henceforth, the σ_{abs} contributed by BC at 450 nm can be derived as:

$$\boldsymbol{\sigma_{\text{abs BC},450}} = \boldsymbol{\sigma_{\text{abs},630}} \cdot \left(\frac{450}{630}\right)^{-AAE_{450/630}} \quad (4)$$

Where the $\sigma_{\text{abs},450}$ and $\sigma_{\text{abs},630}$ were derived using the EMS method with the A2S2 for the airborne measurements and were obtained from the AE33 for the PRG measurements. Then the σ_{abs} of BrC at 450 nm can be estimated as:

$$\boldsymbol{\sigma_{\text{abs BrC},450}} = \boldsymbol{\sigma_{\text{abs},450}} - \boldsymbol{\sigma_{\text{abs BC},450}} \quad (5)$$

To assess the uncertainty associated with the assumed BC AAE, the BrC absorption fraction was also calculated using BC AAE values ranging from 0.8 to 1.2 to provide a sensitivity range. Previous studies also report strongly absorbing BrC species (e.g., tar balls or dark BrC) may also importantly contribute to the absorption at long wavelengths. However, these long-wavelength-absorbing BrC species have been reported predominantly in biomass burning aerosols (Xu et al., 2026), and no evidence of biomass-burning influence was observed during the selected measurement period of the ACROSS campaign in this study. Therefore, although the assumption of negligible BrC absorption at 630 nm may slightly underestimate the BrC

contribution to aerosol absorption at 450 nm, it is unlikely to substantially affect the observed relative variations or the main conclusions of this study.

The Single Scattering Albedo (SSA) at 450 and 630 nm is derived from the ratio between σ_{scat} and σ_{ext} at each wavelength:

$$\boldsymbol{SSA_{\lambda}} = \frac{\sigma_{scat,\lambda}}{\sigma_{ext,\lambda}} \qquad (6)$$

The complex refractive index (CRI) is estimated using a size-integrated optical closure approach based on aerosol size distribution and optical properties measurements (same as the CRI estimation method described in Di Antonio et al. (2025)). Mie theory is applied to calculate the aerosol scattering and absorption coefficients for a range of prescribed CRI, with the real part (n) varying from 1.2 to 1.8 (at 0.01 step) and the imaginary part (k) from 0 to 0.02 (at 0.001 step). For each prescribed CRI pair ($n + ki$), the simulated scattering and absorption coefficients are compared with the corresponding observations, and the root mean square difference (RMSD) is computed as the cost function:

$$\boldsymbol{RMSD} = \sqrt{\left(\frac{\sigma_{scat,model}-\sigma_{scat,measure}}{\sigma_{sca,model}}\right)^2 + \left(\frac{\sigma_{abs,model}-\sigma_{abs,measure}}{\sigma_{abs,model}}\right)^2} \qquad (7)$$

Where $\boldsymbol{\sigma_{scat,model}}$ and $\boldsymbol{\sigma_{scat,measure}}$ represent the modelled and measured scattering coefficient, respectively; $\boldsymbol{\sigma_{abs,model}}$ and $\boldsymbol{\sigma_{abs,measure}}$ represent the modelled and measured absorption coefficient, respectively. The CRI pair that minimizes the RMSD is selected as the optimal solution.

At the PRG site, the optical measurements were constrained to the PM_1 size range. Therefore, the SMPS results were used to determine the size-resolved number concentration (Di Antonio et al., 2025). For the airborne observations, the size distribution was constructed from the combined UHSAS (from ~0.08 to 1 μm) and Sky-OPC (from ~1 to ~10 μm) measurements, ensuring coverage of the full particle size range relevant to A2S2 measurements.

2.5 Paris plume periods identification and transportation age estimation

Paris urban plume intercepts were identified in the airborne measurements based on concurrent and persistent enhancements in both NO_2 and CO mixing ratios above a threshold defined as the flight-specific regional background plus two standard deviations. When SP2 measurements were available, concurrent enhancements in rBC mass concentration within the identified plumes further supported the validity of the is identification approach. The t-test was also applied as a supplementary statistical check to assess whether the identified plume periods exhibited higher tracer concentrations than the corresponding out-plume periods. The background period for each plume was defined as the 5-min interval before and after the plume period, with a 1-min transition interval applied to avoid contamination from the plume. Figure 2(a) presents an example of an identified plume and background period from the Flight A028 on 23rd June, 2022.

The intercepts of the Paris urban plume were further confirmed by a back trajectory analysis. Back trajectories were computed every 15s along the plume period using the UK Met Office Numerical Atmospheric-dispersion Modelling Environment (NAME) model (Jones et al., 2007), driven by meteorological fields from the UK Met Office Unified Model. NAME outputs 24-hour back trajectories on a 0.01° × 0.01° grid by releasing and tracking ensembles of Lagrangian particles, with their historical positions output at 15-min intervals. The 24-hour trajectories are subsequently used to determine whether the sampled air masses have passed over the Greater Paris Region. The wind direction in the meteorological fields was validated against wind direction measurements onboard the aircraft. Figure 2(b) presents the back trajectory results from the same identified plume period from the same flight (Flight A028).

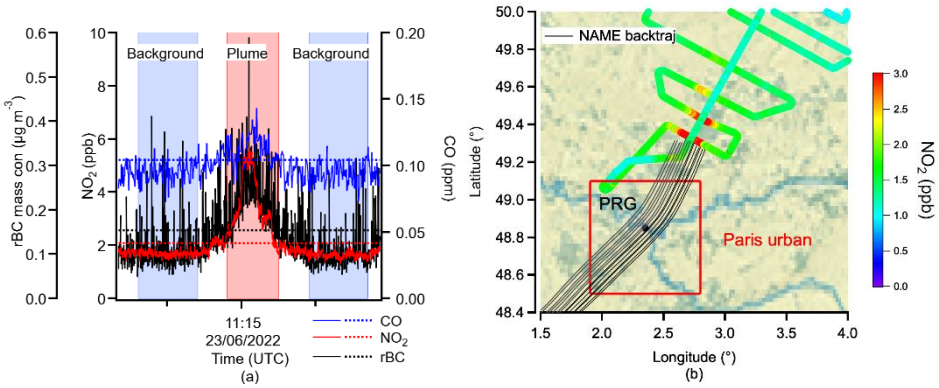

Figure 2. (a) An example of an airborne measured Paris urban plume identified by measured concentrations of NO2 and CO from the Flight A028 on Jun 23rd, 2022. The dashed line indicates the threshold for each plume tracer, defined as the 5th percentile concentration plus twice the standard deviation of the measurements for each flight; (b) Back trajectory analysis for the same plume event. Maps were created from public domain GIS data on Natural Earth (http://www.naturalearthdata.com, last access: 01/04/2026).

Once this criterion satisfied, the transport age was derived from the backward trajectories as the time difference between the airborne plume intercept and the point at which the back-tracked particles reached their closest approach to the PRG measurement site. Only the first two plume intercepts encountered during the zigzag flight transects were considered, with an average estimated transport age of less than 6 h. This selection helps reduce the influence of fresh emissions originating from municipalities or industrial sites surrounding the Greater Paris Region. This approach also enables the identification of the urban plume intercepts in flights with lower aerosol loading (as Flight A031, A033 and A034 presented in Figure 3), when pollutants concentrations became too low due to dilution. Table S2 in the Supplementary Information summarizes the identified plume periods during the airborne measurements together with the corresponding estimated emission times originating from central Paris. All the PRG results presented in this study are based on data selected within the corresponding emission time windows for the plume periods identified in each flight.

Flights including both outbound and inbound plume interceptions are divided into two case studies, labelled (a) and (b), respectively, as they corresponded to distinct emission periods from the Paris urban centre. The outbound interceptions were mainly associated with the morning traffic rush hour (04:00 – 08:00 UTC) at the PRG site, whereas the inbound interceptions were more representative of midday conditions (09:00 – 12:00 UTC).

3. Results and discussions

3.1 Overview of in-Plume and out-plume results from airborne measurements

Figure 3 compares average concentrations of PM_1 (for Flight A028, A032, and A033) or NR-PM_1 (for Flight A027(a), A027(b), A031, A034, and A036) components from the plume period with those from the nearest out-plume background period. The total PM_1 mass concentration from the airborne measurement was determined as the sum of the NR-PM_1 and rBC mass concentration measured by the mAMS and the SP2, respectively. Flights were categorized into high and low aerosol loading cases based on their average PM_1 concentrations, using a threshold of 3 μg m^{-3} derived from the median PM1 mass concentration across all flights. Among all the components, Org dominated the contribution of PM_1 mass concentrations (accounted more than 50% of total PM_1 mass concentration) across all the flights during both in-plume and out-plume periods followed by the SO_4 and pNO_3. According to the flights with available SP2 measurements (A028, A032, and A033), rBC contributed less than 5% to the total PM_1 mass concentration.

Compared with out-plume periods, although total PM_1 mass concentrations showed a statistical increase during in-plume periods (t-test, $p < 0.05$), the magnitude of the increase was modest (< 2 μg m^{-3}). This was primarily due to that the regional background plays an important role in total air mass Beekmann et al. (2015) suggested that regional transport from upwind regions contribute 70% of the fine particles ($PM_{2.5}$) in Paris region on average. The Southwest (SW) Flight A027 exhibited the highest NR-PM_1 concentrations among all flights, consistent with the elevated PM_1 concentrations measured at the Paris suburban site (Rambouillet Forest) during the period dominated by the same north-easterly air mass (Yu et al., 2025), suggesting that north-easterly air masses carried higher particle loadings into the Paris region during this flight.

Compared with previous airborne measurements over other urban regions, observations across Europe (Mcmeeking et al., 2012; Freney et al., 2014; Morgan et al., 2010), Asia (Nault et al., 2018), and Americas (Shingler et al., 2016; Vu et al., 2016; DeCarlo et al., 2008; Shilling et al., 2018), consistently indicate a substantial contribution of Org to total PM_1 mass within downwind urban plumes. In our study, Org accounted for approximately 56.4–70.2% of PM_1 mass under in-plume conditions, compared with 60.6–68.9% under out-plume conditions, indicating the dominant contribution of Org to PM_1 in both the Paris urban plume and the surrounding regional background. Previous studies over Paris (Freney et al., 2014) and London (Mcmeeking et al., 2012) have shown that marine-influenced air masses are typically associated with an enhanced mass

fraction of SO_4. However, our measurements during marine air mass influence periods (A031 and A036) did not exhibit a significant contribution of SO_4 to total PM_1 mass concentrations. This reduced SO_4 contribution was likely attributable to decreased sulfur oxides (SO_x) emissions from shipping activities over the Atlantic Ocean, following the implementation of stricter sulfur regulations by the International Maritime Organization (IMO) in 2020. Yu et al. (2020) estimated that SO_4 emissions from shipping over the Atlantic Ocean declined by more than 80%, resulting in a lower SO_4 contribution in regional air masses advected to the European urban region.

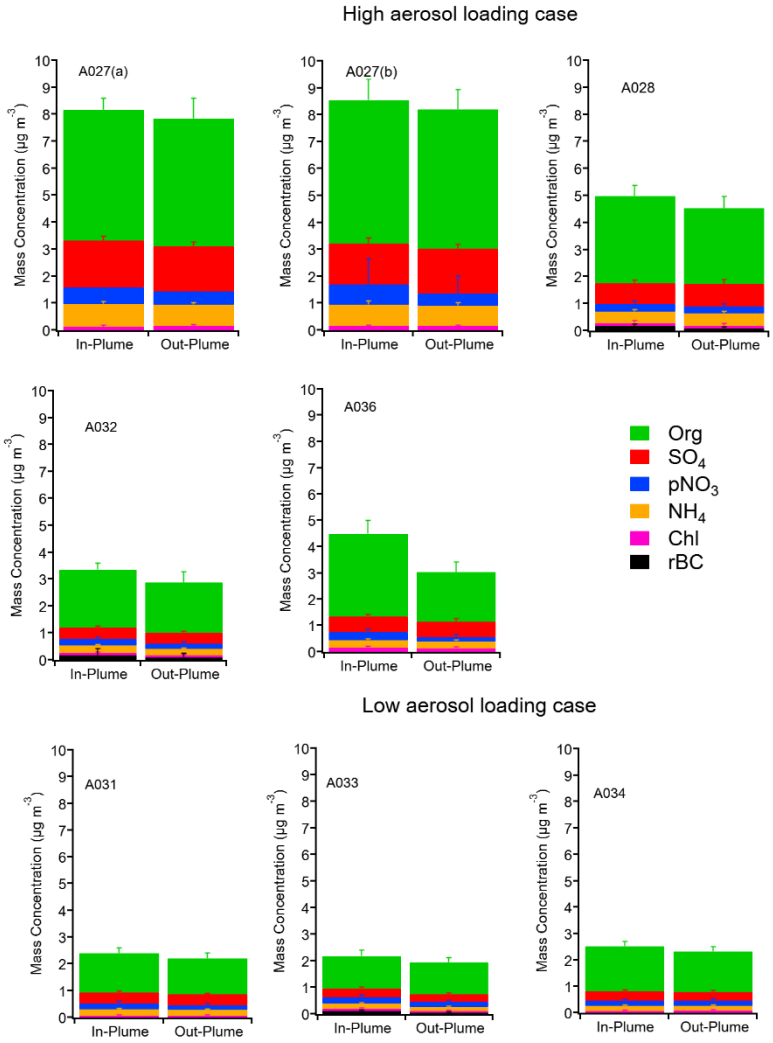

Figure 3. Comparison of average PM_1 or NR-PM_1 component mass concentrations (± standard deviation) during the in-plume period and the nearest out-plume background period. rBC data from the SP2 measurements were available only for Flights A028, A032, and A033; therefore, results were reported as PM_1 for these flights and as NR-PM_1 for the remaining flights. Details of the average mass concentrations of each aerosol component, along with the standard deviation for each flight, are presented in Table S4 in the Supplementary Information.

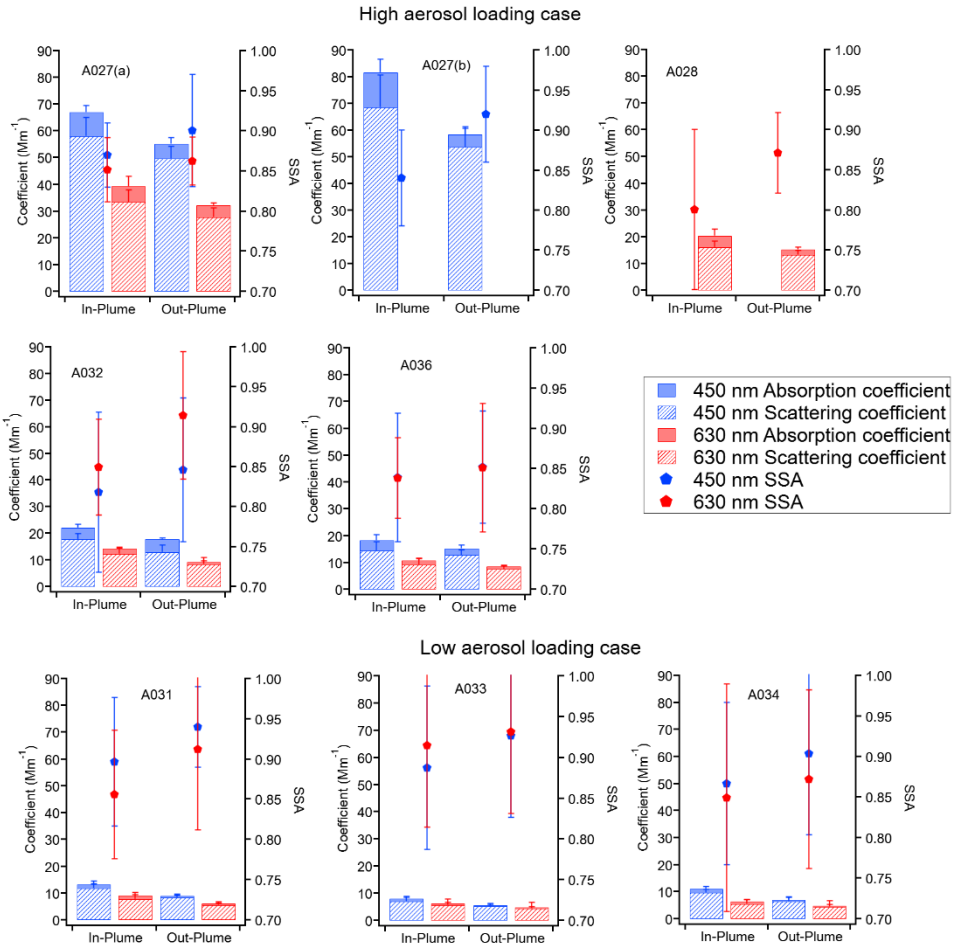

Figure 4. Comparison of average aerosol scattering and absorption coefficients (± standard deviation) at 450 and 630 nm for the in-plume period and the nearest out-plume background period. The corresponding SSA at both wavelengths is also presented for in-plume and out-plume periods. Details of the average σ_{ext}, σ_{scat}, and SSA at both 450 nm and 630 nm, along with their standard deviations for each flight, are presented in Table S5 in the Supplementary Information.

Figure 4 shows the in-plume and out-plume average aerosol scattering and absorption coefficients, along with average SSA, at 450 and 630 nm for all flights. The average in-plume σ_{ext} at 450 and 630 nm was higher than during out-plume periods due to enhanced NR-PM$_1$ levels (t-test, $p < 0.05$). Comparison of For the high aerosol loading periods flights, Flights A032 exhibited lower average SSA at 450 nm than at 630 nm and exhibited higher AAE than SAE, with the differences exceeding the estimated 20% uncertainty in AAE. This is consistent with the higher SSA observed at 630 nm, reflecting a stronger wavelength dependence of absorption than scattering. For Flights A027a and A036, the differences between SAE and AAE were close to the ~20% measurement uncertainty of AAE, indicating comparable wavelength dependences of scattering and absorption and corresponding to relatively small differences in SSA between 450 and 630 nm. During the lower aerosol loading

periods, the wavelength dependence of SSA varied among individual flights. Flights A031 and A034 exhibited lower SSA at 630 nm than at 450 nm, whereas Flight A033 showed the opposite pattern. These spectral patterns were qualitatively consistent with the relative magnitudes of AAE and SAE; however, under low aerosol loading conditions, the optical signals approached the instrumental detection limits, resulting in greater relative uncertainties in the derived optical parameters.

Compared with previous airborne observations over urban regions, the measured σ_{ext} at 630 nm observed in this study was comparable to values observed over the Denver metropolitan area in summer under similar NR-PM_1 aerosol loading levels (σ_{ext} at 630 nm < 20 Mm^{-1} and NR-PM_1 < 10 μg m^{-3} in their study) (Dingle et al., 2016). While the measured SSA observed in this study is close to the average SSA reported within the London urban plume in summer (0.89 and 0.88 at 467 nm and 652 nm, respectively) (Davies et al., 2019), our results indicate stronger absorption at shorter wavelengths in the Paris urban plume compared to London. The average SSA at 450 nm observed in this study is comparable to the boundary-layer average SSA at 440 nm over Beijing during low aerosol loading periods, which ranged from 0.80 to 0.85 (Tian et al., 2020).

3.2 Comparison between airborne and ground-based measurements

3.2.1 Evolution of particle size distribution

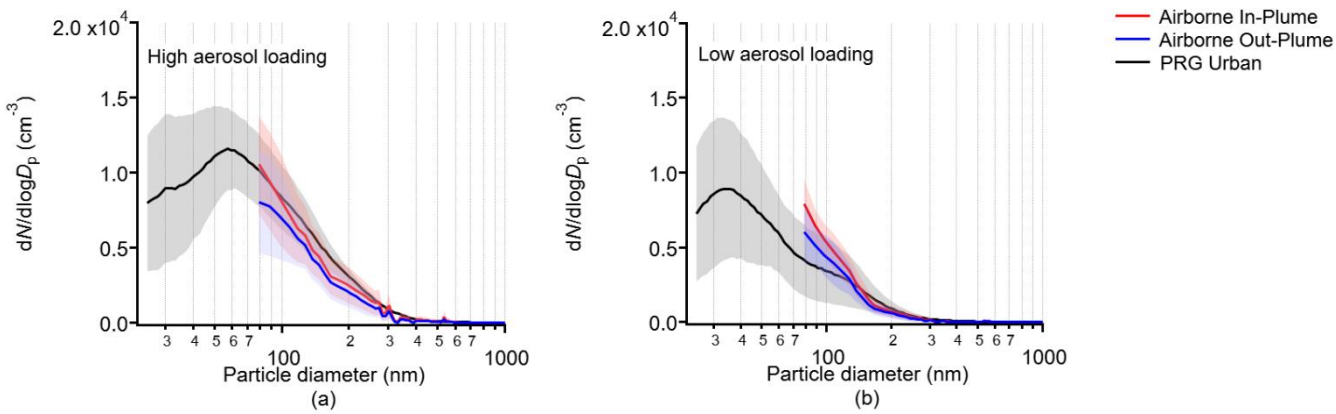

Figure 5. Average particle number size distributions measured by the PRG SMPS (fresh urban emissions) and the airborne UHSAS (in-plume and out-plume periods) during (a) high and (b) low aerosol loading conditions. The shaded area indicates the uncertainty, represented by the standard deviation. PRG results were selected based on the corresponding emission time windows listed in Table S3 in the Supplementary Information.

Figure 5 compares the particle number size distributions measured at the PRG site during the estimated emission periods of the Paris urban plume with those obtained from airborne measurements during in-plume and out-plume periods downwind. During high aerosol loading periods, the particle size distributions at the PRG urban site exhibited a modal peak between 50

and 60 nm, whereas during low aerosol loading periods the peak shifted to smaller diameters, centred at approximately between 30 and 40 nm.

Downwind aircraft measurements showed an enhancement in particle number concentrations in the 80–200 nm size range during in-plume periods compared to out-plume periods. particle number concentrations in the overlapping 80–200 nm size range remained of a similar magnitude despite plume dilution, indicating that the 80–200 nm size range remained a substantial fraction of the particle population during plume transport. In the Greater London region, enhanced contributions from particles in the 100–200 nm size range have been observed at downwind suburban sites (Beddows et al., 2015; Harrison et al., 2019). Likewise, Cirino et al. (2018) reported enhanced particle number concentrations in the 100–200 nm size range in aged urban plumes over downwind suburban areas in South America. The increase in particle number concentration in the 80–200 nm size range resulted in only a modest yet statistically increase in particle volume under in-plume conditions compared to out-plume conditions downwind of Paris (t-test, $p < 0.05$). The average volume concentration was 5.79 ($\pm$3.34) $\mu m^3\ cm^{-3}$ for in-plume period and 4.54 ($\pm$2.43) $\mu m^3\ cm^{-3}$ for out-plume period during the high aerosol loading and was 2.47 ($\pm$0.86) $\mu m^3\ cm^{-3}$ for in-plume period and 1.93 ($\pm$0.72) $\mu m^3\ cm^{-3}$ for out-plume period during the low aerosol loading periods. This modest increase in particle volume was consistent with the PM_1 mass concentrations shown in Figure 3, which also exhibited only a limited enhancement between in-plume and out-plume periods despite the increases in the urban plume tracers, including NO_2 and CO mixing ratios and rBC mass concentration. Although rBC exhibited the largest relative in-plume enhancement among the measured PM_1 components, it accounted for only a small fraction of the total PM_1 mass and was characterized by a relatively low background concentration. In contrast, PM_1 mass was dominated by Org and secondary inorganic species, which exhibited much smaller relative enhancements because of their larger regional background contributions. Consequently, the overall increase in PM_1 mass was considerably smaller than that observed for the gas-phase tracers and rBC. Using the overlapping particle size range common to both the PRG site and the downwind airborne measurements (80–1000 nm), the average volume-effective radius at PRG was 314 (±31) nm during high aerosol loading periods and 323 (±37) nm during low aerosol loading periods, compared with 318 (±63) nm and 308 (±103) nm, respectively, in the downwind plume. These differences were not statistically significant (t-test, $p > 0.05$), indicating that no statistically significant change in the volume-effective size was detected within the 80–1000 nm size range between the PRG site and the downwind plume.

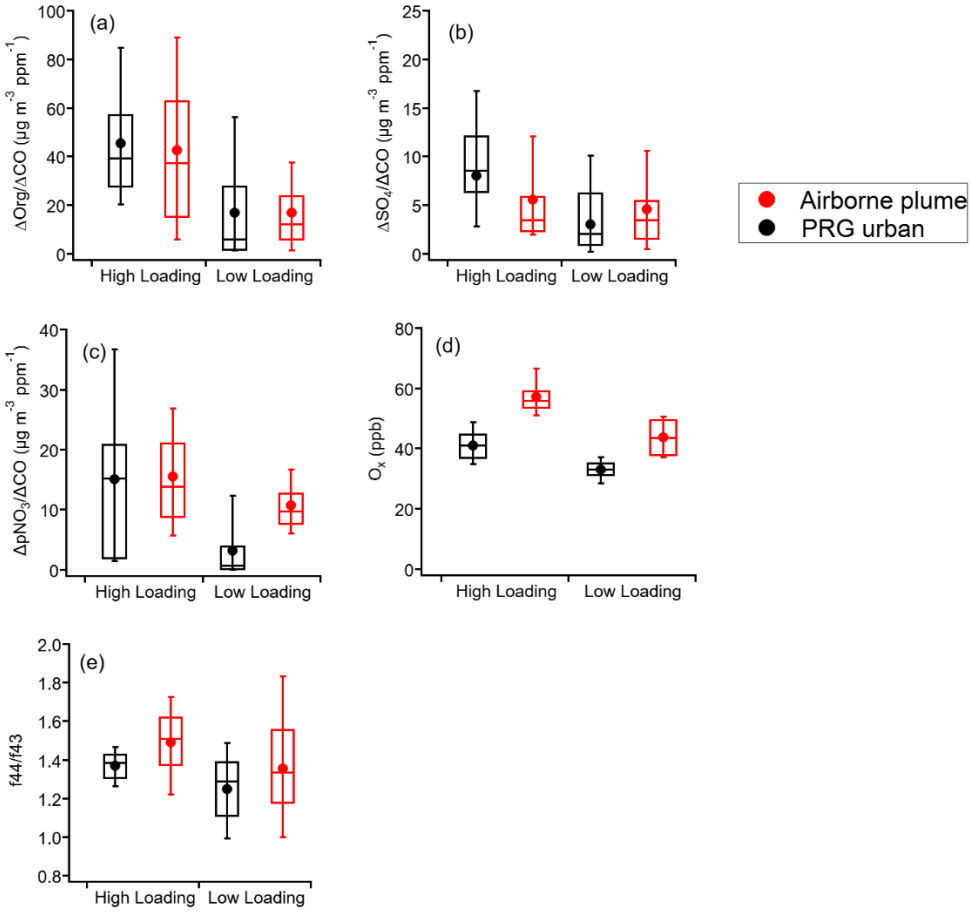

Figure 6. Relative enhancements of (a) organic aerosol (Org), (b) sulfate (SO4), (c) nitrate (NO3); (d) Ox (NO2 + O3) concentration, (e) f44/f43 measured at the PRG urban site and in the downwind urban plume from airborne observations during high and low aerosol loading periods. Results are normalised to ΔCO to evaluate the relative enhancement of each species with respect to primary urban emissions. Boxes show the interquartile range (25th–75th percentiles), whiskers indicate the 10th–90th percentiles, the horizontal line represents the median, and the dots denote the mean values.

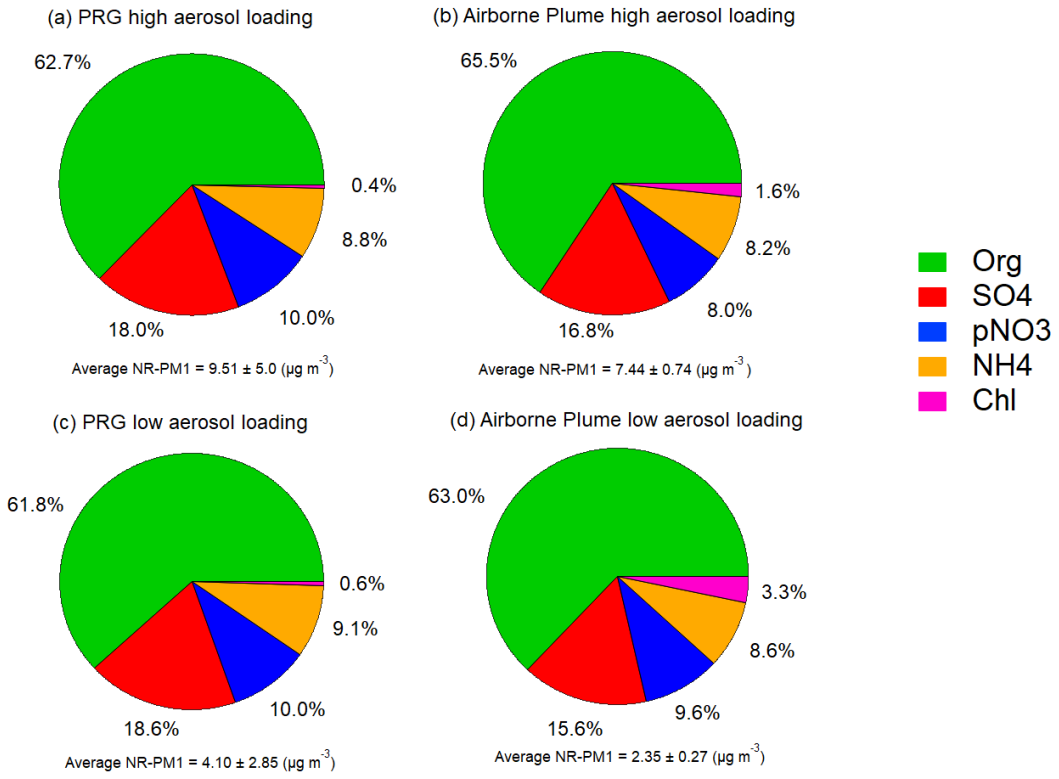

Figure 7. Mass fraction of NR-PM$_1$ components measured at (a)(c) PRG urban site and (b)(d) downwind urban plume derived from airborne results during high- and low- aerosol loading periods. The uncertainty in the average NR-PM$_1$ represents the standard deviation.

3.2.2 Variation of aerosol components

Figures 6 and 7 show the normalised NR-PM$_1$ component concentrations and O_x ($NO_2 + O_3$), as well as the mass fractions of NR-PM$_1$ components measured at the PRG urban site and in the downwind urban plume from airborne observations during high and low aerosol loading periods. Results in Figure 6 are normalised to ΔCO to evaluate the relative enhancement of each species with respect to primary urban emissions, using CO as a relatively conserved tracer of anthropogenic emissions during short-range plume transport.

The average Ox concentrations at the PRG urban site differed only slightly between the two aerosol-loading regimes, although the t-test indicated a statistically significant difference ($p < 0.05$). This relatively small difference suggests that the initial photochemical conditions were broadly comparable between the two regimes. Flight A027b, conducted around noon under

potentially stronger photochemical conditions, was included in the analysis. Excluding A027b changed the mean downwind Ox concentration by only ~5% and did not alter the overall urban-to-downwind pattern, indicating that this flight had a limited influence on the observed O_x differences. The downwind airborne measurements showed higher average O_x concentrations than those observed at the PRG site (t-test, $p < 0.05$). As Ox is presented here as an absolute concentration rather than normalized to ΔCO, this difference is interpreted as reflecting different photochemical conditions between the urban and downwind air masses rather than as a quantitative measure of photochemical Ox production during transport. The higher average f44/f43 ratio observed downwind (t-test, $p < 0.05$) was also consistent with a greater relative contribution of more oxidized Org. However, these compositional changes were not accompanied by a substantial increase in aerosol mass relative to CO during the early stages of plume aging across different aerosol loading regimes. The average ΔOrg/ΔCO showed limited urban-to-downwind changes across different aerosol loading regimes after ~2–6 h of transport, suggesting limited net enhancement of secondary aerosol mass relative to CO. The mass fraction of aerosol components also shows limited variations, and Org was the dominant NR-PM_1 aerosol components both at the urban site and downwind. Within the airborne measurements alone (as shown in Figure S6 in the Supplementary Information and also in Velazquez-Garcia et al. (2026b)), ΔOrg/ΔCO exhibited a tendency to increase with transport time, suggesting progressive Org mass concentration enhancement within the downwind plume. Nevertheless, the magnitude of this increase was relatively small compared with the overall urban-to-downwind variability and did not result in a clear enhancement relative to the PRG observations. No consistent enhancement in $\Delta SO_4/\Delta CO$ was observed from the PRG site to the downwind plume. The average $\Delta SO_4/\Delta CO$ was lower downwind under high aerosol loading, whereas only a limited difference was observed under low aerosol loading, indicating no clear net accumulation of sulfate relative to CO during the investigated transport period. This may be due to limited precursor availability within the urban plume, as SO_x emissions have declined across European urban areas over the past decades (Ciarelli et al., 2019; Tsimpidi et al., 2025). $\Delta pNO_3/\Delta CO$ showed limited difference between the PRG and downwind measurements under high aerosol loading, whereas higher values were observed downwind under low aerosol loading. This may be partly attributed to enhanced evaporation of particulate nitrate to the gas phase during plume aging under high aerosol loading conditions, when temperatures were higher than during the low aerosol loading periods. The average temperature measured onboard the aircraft was higher during the high aerosol loading periods (18.2 ± 1.6 °C) compared to the low aerosol loading periods (15.7 ± 1.7 °C) (t-test, $p < 0.05$). Although the average RH measured onboard the aircraft was also higher during the high aerosol loading period (58 ± 11%) than during the low aerosol loading period (52 ± 5%) (t-test, $p < 0.05$), the higher temperatures likely played a key role in promoting the volatilization of ammonium nitrate, thereby reducing pNO_3 formation efficiency. This is similar to prior airborne studies, such as DeCarlo et al. (2008), that observed decreases of pNO_3 as the urban plume over Mexico City was transported away from the city core.

3.3 Impacts of plume aging on aerosol optical properties

3.3.1 Variation of CRI and SSA

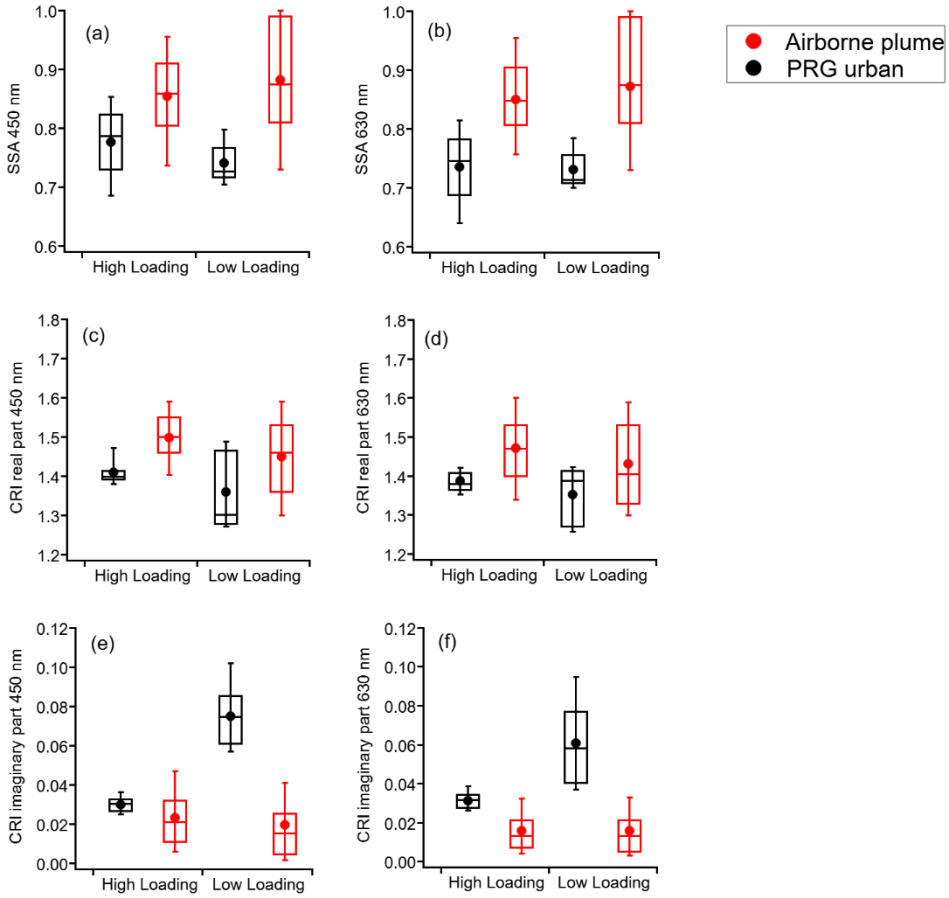

Figure 8. SSA at (a) 450 nm and (b) 630 nm, and complex refractive index (CRI) at (c, d) the real part and (e, f) the imaginary part at 450 nm and 630 nm, respectively. Results are shown for PRG site measurements and airborne observations during high and low aerosol loading periods. Boxes show the interquartile range (25th–75th percentiles), whiskers indicate the 10th–90th percentiles, the horizontal line represents the median, and the dots denote the mean values.

Figure 8 presents the comparison between the SSA and CRI in fresh urban plume from the PRG urban measurements and the aged plume measured by the aircraft at different aerosol loading levels. Downwind Paris urban plume, the low aerosol loading periods-plumes average SSA was statistically higher than that observed during high aerosol loading periods in the airborne measurements (t-test $p < 0.05$), reflecting a relatively weaker contribution from absorbing components (Figure 8(a)(b)).

At the PRG site, no statistically significant difference was observed in the average SSA at 630 nm between aerosol loading regimes (t-test, $p > 0.05$, Figure 8(b)), whereas the average SSA at 450 nm was slightly lower during low aerosol loading periods (t-test, $p < 0.05$, Figure 8(a)). Consistent with this behaviour, the imaginary part of the CRI increased at both wavelengths during low aerosol loading periods compared to high aerosol loading periods (Figure 8(e)(f)). However, the lower aerosol loadings during these periods resulted in weaker optical signals and consequently greater uncertainty and variability in the CRI retrieval, which may partly contribute to the relatively high imaginary and low real CRI values. This increased variability is reflected in the broader 25th–75th percentile ranges of the retrieved CRI during low aerosol loading periods, as shown in Figure 8. The PRG measurements also showed lower f44/f43 ratios during the low aerosol loading than during the high aerosol loading periods, indicating relatively less oxidized organic aerosol. This is qualitatively consistent with the lower real part of the CRI. The tendency toward a higher imaginary CRI may also reflect a greater relative influence of local emissions at PRG. The proximity of the PRG site to emission sources and the inclusion of morning rush-hour emissions (04:00–08:00 UTC) in the selected plume emission period are consistent with the diurnal analysis presented in Di Antonio et al. (2025). During low aerosol loading periods, the reduced influence of regionally transported NR-PM_1 may increase the relative contribution of local traffic emissions, potentially contributing to the higher imaginary part of the CRI despite the overall cleaner conditions. In contrast, airborne measurements downwind did not show the same trend in the imaginary part of the CRI. While the real part of the CRI during the low aerosol loading periods was lower than that observed during high aerosol loading periods downwind of the Paris urban plume (t-test, $p < 0.05$, Figure 8(c)(d)), the imaginary part remained statistically similar (t-test, $p > 0.05$, Figure 8(e)(f)). This suggests that the variation in the imaginary part of the CRI at the PRG site during low aerosol loading periods was likely driven by local sources.

The average SSA showed differences between measurements at the PRG site and the downwind aged plume. At both 450 and 630 nm, the average SSA increased from below 0.8 in the fresh urban emissions at PRG to above 0.8 in the aged Paris urban plume from the aircraft measurements (Figure 8(a)(b)). This increase in SSA indicates a transition of the aerosol population from a more absorption-dominated regime toward a more scattering-dominated one. This variation of SSA is consistent with previous airborne measurements downwind of Los Angeles (Langridge et al., 2012) and London (Mcmeeking et al., 2012), which also report a progressive transition toward more scattering-dominated aerosol populations. Consistent with the SSA evolution, the average CRI also changed between fresh and aged plume conditions. At PRG, the average real part of the CRI was approximately 1.35 to 1.4 (Figure 8(c)(d)), while the average imaginary part ranged from 0.03 to 0.08 at both 450 and 630 nm (Figure 8(e)(f)). In contrast, airborne measurements of the aged plume showed a higher average real part (~1.45–1.50, Figure 8(c)(d)) together with a lower average imaginary part (~0.015–0.02, Figure 8(e)(f)) at both wavelengths (t-test $p < 0.05$).

These variations in SSA and CRI may be driven by changes in aerosol chemical composition during plume aging. In particular, the decrease in the imaginary part of the CRI at both wavelengths suggests a reduced relative contribution from strongly absorbing particles. As presented in Figure S2 in the Supplementary Information, for flights with SP2 measurements available,

the rBC mass fraction decreased downwind of the urban plume during both high and low aerosol loading periods. This decrease of rBC mass fraction was more pronounced during the low aerosol loading period, consistent with the larger reduction in the imaginary part observed under these conditions. Observations across diverse environments globally have shown that a reduction in BC mass fraction leads to an increase in SSA at both short and long wavelengths. (Eom et al., 2025). Ground-based measurements during the ACROSS project period also indicate that the imaginary part of the CRI was strongly associated with BC (reported as eBC in that study) mass fraction, and its reduction at the downwind suburban forest sites led to a lower imaginary part compared to the PRG site (Di Antonio et al., 2025). Meanwhile, given the substantial contribution of Org to NR-PM_1 at both PRG site and downwind urban plume, the increase in the real part of the bulk aerosol CRI may be largely driven by changes in the optical properties of Org during plume aging. As shown in the supplementary, estimates based on measured NR-PM_1 species mass concentrations indicate that the average real part of the Org CRI increased from fresh urban emissions at the PRG site to the more aged urban plume sampled downwind during the airborne measurements. Similar behaviour has been reported in previous studies. Shen et al. (2025) reported that an increasing fraction of SOA within total Org may lead to an increase in the average real part of the Org CRI in the urban environment. Flores et al. (2014) also observed an increase in the real part of the CRI during laboratory photooxidation of mixed biogenic and anthropogenic VOCs. In their experiments, the real part of the CRI increased from ~1.46 to ~1.51 at 405 nm after a photochemical aging within 4h. As Org contributes substantially to NR-PM_1, the higher real part of the CRI associated with photo-oxidized Org may drive the increase in the population-averaged CRI real part downwind of the urban plume.

3.3.2 Variation of the wavelength dependence of aerosol optical properties

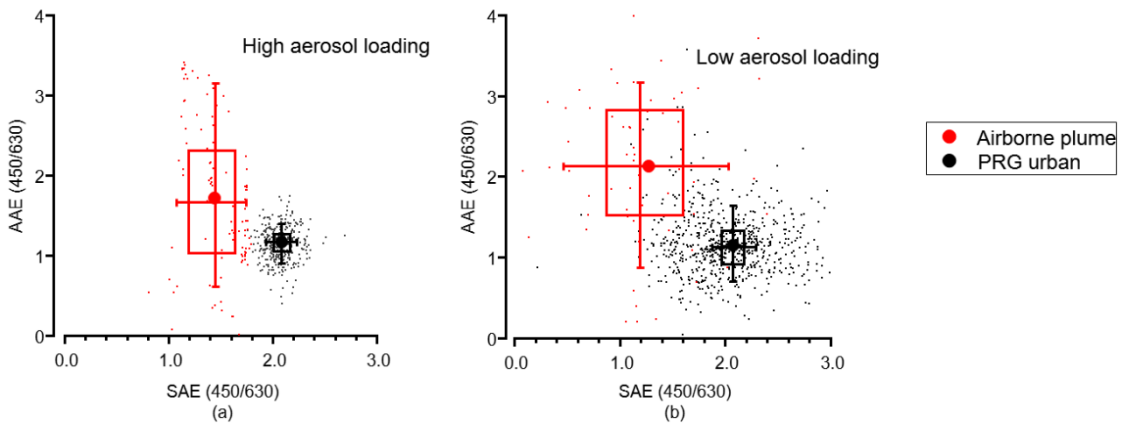

Figure 9. AAE versus SAE for the airborne-measured Paris urban plume and the corresponding ground-based measurements at the PRG site at (a) high aerosol loading period and (b)low aerosol loading period. Boxes show the interquartile range (25th–75th percentiles), whiskers indicate the 10th–90th percentiles, the horizontal line represents the median, and the dots denote the mean values.

Figure 9 compares the AAE and SAE derived from airborne and PRG ground-based measurements. Owing to the lower aerosol concentrations in the airborne observations, particularly during the low aerosol loading periods, the airborne AAE and SAE results exhibited larger variability compared to the PRG urban measurements. Therefore, the impact of differing measurement size cutoffs was likely minor. The spectral dependence of both absorption and scattering varied between the PRG site and the downwind airborne measurements. As shown in Figure 9, the average AAE at the PRG site was close to 1, while the average SAE was approximately 2 under both aerosol-loading regimes. The mean values were of comparable magnitude between the two aerosol loading regimes, while the t-test did not detect a statistically significant difference ($p > 0.05$).

For the downwind airborne measurements, the average AAE was approximately 2 and the average SAE was around 1.5 under both aerosol-loading regimes. The observed difference in average AAE between the PRG site and the downwind airborne measurements exceeded the A2S2 measurement uncertainty in AAE (~20%), while the t-test also indicated a statistically significant difference ($p < 0.05$). Within the downwind plume sampled by the aircraft, the spectral dependence of aerosol absorption and scattering evolved with plume aging. As shown in Figure S5 in the Supplementary Information and in Velazquez-Garcia et al. (2026b), AAE exhibited an increasing trend with estimated plume transport age, particularly during the higher aerosol loading periods, indicating a progressively stronger wavelength dependence of aerosol absorption during downwind transport. During the lower aerosol loading periods, AAE showed substantially greater variability, while the average values remained higher than those observed at the PRG urban site.

Several factors likely contributed to the observed urban-to-downwind changes in the spectral dependence of aerosol absorption and scattering. The reduction in rBC mass fraction downwind of the Paris urban plume led to a fractional decrease in its contribution to total light absorption compared to PRG site. Meanwhile, the increased relative contribution of more oxidized Org coincided with an enhanced BrC absorption contribution, suggesting that changes in Org composition may have contributed to the observed changes in wavelength-dependent absorption. The average BrC absorption fraction was 15.7 (± 17.7) % during high aerosol loading periods and 8.9 (± 6.9) % during low aerosol loading periods at the PRG site, with sensitivity ranges of 11.9–18.1% and 6.9–12.5%, respectively, when the assumed BC AAE was varied from 0.8 to 1.2. to 39.1 (±20.8) % and 42.0 (±31.1) %, respectively, within the downwind plume. Within the downwind plume, the average BrC absorption fractions increased to 39.1 (±20.8) % and 42.0 (±31.1) %, with corresponding sensitivity ranges of 36.8–41.1% and 45.0–47.2%, respectively, when the assumed rBC AAE was varied from 0.8 to 1.2. This enhanced BrC contribution shifted the spectral absorption toward shorter wavelengths, resulting in higher average AAE in the downwind plume. This interpretation is consistent with measurements on the ground during the ACROSS campaign period (Yu et al., 2025), which reports an increase of BrC absorption fraction at short wavelength to summertime light absorption associated with active secondary processes. Similar trend was also observed in the comparison between Paris urban site and suburban sites in Di Antonio et al. (2025). During the campaign, the downwind suburban sites had relatively higher BrC absorption fraction compared to the Paris urban site. The observed decrease in average SAE may partially attributed to differences in the upper

size cutoffs used in the airborne (10 μm) and ground-based PRG (1 μm) measurements. However, the influence of coarse mode particles was expected to be limited, as indicated by the consistently high average SAE values (>1). Furthermore, although the volume-effective particle size showed little variation within the 80–1000 nm range between the PRG site and the downwind plume, indicating limited particle growth within this size range, potential size-resolved compositional changes (Zaveri et al., 2010) cannot be excluded and may have contributed to the observed decrease in average SAE.

3.3.3 Comparison of CRI at the urban site and downwind with previous measurements

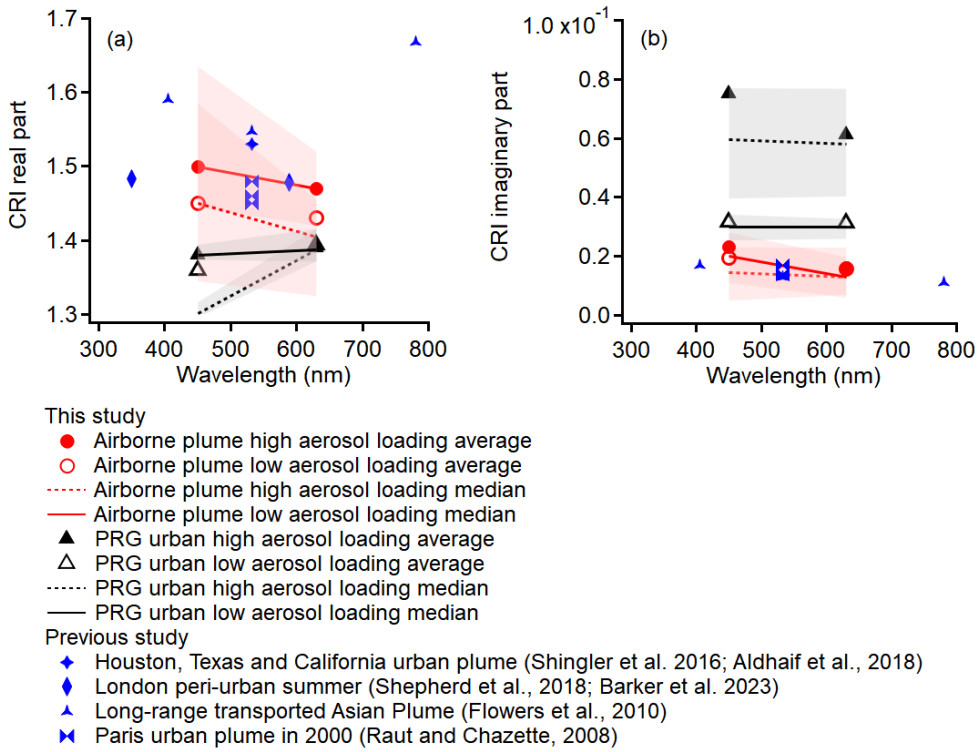

Figure 10. Comparison of CRI (a) real part and (b) imaginary part derived from this study and other urban plume characterisation studies (Shingler et al., 2016; Aldhaif et al., 2018; Shepherd et al., 2018; Barker et al., 2023; Flowers et al., 2010; Raut and Chazette, 2008). Shaded area shows the interquartile range (25th–75th percentiles)

Figure 10 compares the average CRI measured in this study with values reported in previous urban plume characterisation studies. Our results suggest that aerosols in urban environments dominated by primary emissions exhibit lower real and higher imaginary parts of the CRI, whereas downwind regions with stronger secondary contributions show the opposite pattern. A similar trend has also been observed in urban areas in China, where lower CRI real part values of NR-PM_1 are associated with

stronger primary emissions, whereas higher values are linked to greater secondary components contributions (Wu et al., 2021; Shen et al., 2025).

The real part of the CRI measured in London during summer is comparable to the aircraft observations downwind Paris urban plume but higher than the PRG urban measurements, which may reflect the peri-urban nature of the sampling locations and the influence of more aged urban plumes in their study (Shepherd et al., 2018). Both the real and imaginary parts of the CRI observed in our study are slightly higher than those reported by airborne measurements conducted closer to the Paris region in 2000 (Raut and Chazette, 2008). This difference is likely due to the more aged aerosols in our study, which again is consistent with our observed changes with plume age. The real part of the CRI observed downwind of American megacities is higher than that measured in this study, likely due to a larger contribution from secondary inorganic components with higher CRI real part in their observations (Aldhaif et al., 2018; Shingler et al., 2016). Flowers et al. (2010) reports CRI values for long-range transported Asian plumes measured at a remote site, which exhibit a higher real part and a lower imaginary part than those observed in the relatively early aged urban plumes investigated here and in previous studies. These comparison results highlight the dynamic nature of the CRI, which evolves with aerosol composition and chemical aging. Consequently, assuming a static CRI for either bulk aerosol or individual components, particularly the Org fraction, represents an oversimplification and may introduce uncertainties in model simulations or satellite retrievals (Levy et al., 2007; Herrera et al., 2022; Curci et al., 2019). A dynamic parametrization that accounts for atmospheric processing (e.g. (Konovalov et al., 2021; Drugé et al., 2022; Jiang et al., 2024)) would therefore provide a more realistic representation of aerosol optical properties.

Conclusions

In this study, we combined airborne and ground-based observations over the Paris region to characterise urban-to-downwind differences in aerosol physicochemical and optical properties, with downwind observations sampling the urban plume at estimated atmospheric ages of approximately 2–6 hours. Measurements showed that the Paris urban plume was associated with enhanced particle number concentrations in the 80–200 nm size range during downwind transport. Organic aerosol (Org) mass concentrations showed only limited variation downwind, while the relative contribution of more oxidized Org increased. Secondary inorganic species contributed a smaller fraction of PM_1 compared to previous European airborne studies of urban plumes (Mcmeeking et al., 2012; Freney et al., 2014), reflecting recent changes in anthropogenic pollutant emissions in European urban regions (Yu et al., 2020; Tsimpidi et al., 2025; Ciarelli et al., 2019). The downwind aerosol population exhibited more scattering-dominated optical properties than the urban aerosol. The average SSA downwind the Paris urban plume increased at both 450 and 630 nm, consistently with the increase in the real part of the CRI ~1.35–1.40 at the PRG site to ~1.45–1.50 in the aged urban plume downwind, indicating enhanced light scattering, while the imaginary part decreased from ~0.03–0.08 to ~0.015–0.02, reflecting a reduced contribution to light absorption. The CRI measured downwind of the Paris urban plume falls within the range reported for downwind urban plumes and suburban regions (Shingler et al., 2016; Aldhaif et al., 2018; Shepherd et al., 2018; Barker et al., 2023; Raut and Chazette, 2008). The urban-to-downwind differences

in aerosol optical properties were accompanied by a lower rBC mass fraction and higher AAE downwind, consistent with a reduced relative importance of rBC to aerosol light absorption and more scattering-dominated aerosol properties (Di Antonio et al., 2025; Eom et al., 2025). The increase in average AAE in the downwind urban plume indicates a greater fractional contribution of BrC to short-wavelength absorption; however, this increase appears insufficient to offset the overall decrease in absorption and the concurrent increase in scattering. The observed decrease in average SAE in the downwind Paris urban plume suggested a larger relative contribution of larger particles to scattering, potentially due to differences in size cutoffs on different measurement platform and/or size-resolved compositional changes. Incorporating size-resolved compositional observations in future work could help further investigate how compositional evolution across different particle sizes influences the observed optical properties.

In summary, our observations reveal systematic urban-to-downwind differences in aerosol physicochemical and optical properties, consistent with a greater influence of secondary atmospheric processing in the downwind plume compared with the urban site. Such differences may not be fully represented in some atmospheric models and satellite retrieval algorithms that rely on fixed CRI values and simplified aerosol optical assumptions. While recent model and satellite retrieval studies (e.g. (Drugé et al., 2022; Jiang et al., 2024)) have introduced dynamic parameterizations to account for atmospheric processing of aerosol optical properties, substantial uncertainties remain in key optical parameters such as SSA (Li et al., 2022a). In-situ measurements are therefore essential to provide observational constraints, particularly in the context of recent changes in global anthropogenic emissions (Li et al., 2023). To the best of our knowledge, this study represents one of the few post-2017 airborne investigations of aerosol physicochemical properties over a European megacity. The relative variations in the derived CRI and observed SSA provide useful observational constraints for improving the representation of aerosol optical properties in chemical transport models and remote-sensing retrievals.

Data availability

Processed ACROSS flight campaign data are archived at ACROSS AERIS: https://across.aeris-data.fr/ (last accessed 21/03/2026). AIRPARIF data is available from: https://www.airparif.fr/ (last access 11/12/2025).

Author Contributions

CC, PF and VM designed the ACROSS-AO aircraft campaign. CY and PFD operated the mAMS instrument on board the ATR-42 aircraft and performed the associated data analysis, together with BAN. CY conducted the A2S2 measurements on board the ATR-42 and performed the associated data analysis. EA and PDC operated the TD-LIF instrument on the ATR-42 aircraft and performed the associated the data analysis. CD, ST, and TB operated the SP2 instrument on board the ATR-42 aircraft and AVG performed the data analysis. EP, KT, MC, NG, and TB contributed to the modification and configuration of instruments on board the ATR-42 aircraft. DLP, KT, AB, CC, and VM contributed to the airborne experiment. LDA, CDB,

AG, AB, BDA and JK conducted the PRG experiment and analysed the data. CY and HW performed the NAME back trajectory analysis. LDA, MB, GS, and GF provided meteorological and chemical forecast for the flight campaign. CY and PF led the data analysis and drafted the manuscript. All co-authors contributed to the interpretation of the results and provided comments on the manuscript.

Competing interests

At least one of the (co-)authors is a member of the editorial board of *Atmospheric Chemistry and Physics*. The authors have no other competing interests to declare.

Acknowledgment

Airborne data was obtained using the aircraft managed by Safire, the French facility for airborne research, an infrastructure of the French National Center for Scientific Research (CNRS), Météo-France and the French National Center for Space Studies (CNES). The authors wish to thank AERIS (https://www.aeris-data.fr/, last access: 11/12/2025), the French centre for atmospheric data and service, for providing the campaign website and organizing the curation and open distribution of the ACROSS data. Chenjie Yu would like to acknowledge the Marie Skłodowska-Curie COFUND Paris Regional Postdoctoral Fellowship program supported by the Paris Region. The participation of Peter F. DeCarlo to the ACROSS field campaign was funded by the Invited Professor program of the Université Paris Est Créteil. A. Velazquez Garcia's work is supported by the ANR (ANR-20-CE01-0010 and ANR-24-CE01-3132) and Météo-France. Contributions to the PRG set up and measurements by S. Chevaillier, C. Gaimoz, A. Feron. P. Zapf, F. Maisonneuve, G. Močnik, O. Favez, L. Hawkins, S. Riley, and D. Pronovost are gratefully acknowledged. The ACROSS Forecasting team (LISA, SAFIRE, Météo-France) is acknowledged for providing meteorological and chemical forecast supporting the choices of specific predefined flight paths. Special thanks to James D. Allan (University of Manchester) for the valuable discussions and suggestions contributing to this study.

Financial support

Airborne measurements using the Safire ATR-42 aircraft were supported by the ACROSS project, which benefits from French state aid (ANR – “Investissements d’avenir”); References: ANR-17-MPGA-0002 and ANR-20-CE01-0010. Measurements conducted at PRG site was supported by the French National program LEFE (Les Enveloppes Fluides et l’Environnement) of the CNRS/INSU (Centre National de la Recherche Scientifique/Institut National des Sciences de L’Univers) in the framework of ACROSS-GO project. This research also receives funding from the European Union’s Horizon 2020 research and innovation programme under the Marie Skłodowska-Curie grant agreement n° 945298.

Reference

Aldhaif, A. M., Stahl, C., Braun, R. A., Moghaddam, M. A., Shingler, T., Crosbie, E., Sawamura, P., Dadashazar, H., Ziemba, L., Jimenez, J. L., Campuzano-Jost, P., and Sorooshian, A.: Characterization of the Real Part of Dry Aerosol Refractive Index Over North America From the Surface to 12 km, Journal of Geophysical Research: Atmospheres, 123, 8283–8300, https://doi.org/10.1029/2018JD028504, 2018.

Barker, C. R., Poole, M. L., Wilkinson, M., Morison, J., Wilson, A., Little, G., Stuckey, E. J., Welbourn, R. J. L., Ward, A. D., and King, M. D.: Ultraviolet refractive index values of organic aerosol extracted from deciduous forestry, urban and marine environments, Environmental Science: Atmospheres, 3, 1008–1024, 10.1039/D3EA00005B, 2023.

Baron, P. A. and Willeke, K.: Aerosol Measurement: Principles, Techniques, and Applications: Second Edition [2001], John Wiley and Sons2001.

Beddows, D. C. S., Harrison, R. M., Green, D. C., and Fuller, G. W.: Receptor modelling of both particle composition and size distribution from a background site in London, UK, Atmos. Chem. Phys., 15, 10107–10125, 10.5194/acp-15-10107-2015, 2015.

Beekmann, M., Prévôt, A. S. H., Drewnick, F., Sciare, J., Pandis, S. N., Denier van der Gon, H. A. C., Crippa, M., Freutel, F., Poulain, L., Ghersi, V., Rodriguez, E., Beirle, S., Zotter, P., von der Weiden-Reinmüller, S. L., Bressi, M., Fountoukis, C., Petetin, H., Szidat, S., Schneider, J., Rosso, A., El Haddad, I., Megaritis, A., Zhang, Q. J., Michoud, V., Slowik, J. G., Moukhtar, S., Kolmonen, P., Stohl, A., Eckhardt, S., Borbon, A., Gros, V., Marchand, N., Jaffrezo, J. L., Schwarzenboeck, A., Colomb, A., Wiedensohler, A., Borrmann, S., Lawrence, M., Baklanov, A., and Baltensperger, U.: In situ, satellite measurement and model evidence on the dominant regional contribution to fine particulate matter levels in the Paris megacity, Atmos. Chem. Phys., 15, 9577–9591, 10.5194/acp-15-9577-2015, 2015.

Bond, T. C., Doherty, S. J., Fahey, D. W., Forster, P. M., Berntsen, T., DeAngelo, B. J., Flanner, M. G., Ghan, S., Kärcher, B., Koch, D., Kinne, S., Kondo, Y., Quinn, P. K., Sarofim, M. C., Schultz, M. G., Schulz, M., Venkataraman, C., Zhang, H., Zhang, S., Bellouin, N., Guttikunda, S. K., Hopke, P. K., Jacobson, M. Z., Kaiser, J. W., Klimont, Z., Lohmann, U., Schwarz, J. P., Shindell, D., Storelvmo, T., Warren, S. G., and Zender, C. S.: Bounding the role of black carbon in the climate system: A scientific assessment, Journal of Geophysical Research: Atmospheres, 118, 5380–5552, https://doi.org/10.1002/jgrd.50171, 2013.

Brown, H., Liu, X., Pokhrel, R., Murphy, S., Lu, Z., Saleh, R., Mielonen, T., Kokkola, H., Bergman, T., Myhre, G., Skeie, R. B., Watson-Paris, D., Stier, P., Johnson, B., Bellouin, N., Schulz, M., Vakkari, V., Beukes, J. P., van Zyl, P. G., Liu, S., and Chand, D.: Biomass burning aerosols in most climate models are too absorbing, Nature Communications, 12, 277, 10.1038/s41467-020-20482-9, 2021.

Cantrell, C. and Michoud, V.: An Experiment to Study Atmospheric Oxidation Chemistry and Physics of Mixed Anthropogenic–Biogenic Air Masses in the Greater Paris Area, Bulletin of the American Meteorological Society, 103, 599–603, https://doi.org/10.1175/BAMS-D-21-0115.1, 2022.

Capes, G., Johnson, B., McFiggans, G., Williams, P. I., Haywood, J., and Coe, H.: Aging of biomass burning aerosols over West Africa: Aircraft measurements of chemical composition, microphysical properties, and emission ratios, Journal of Geophysical Research: Atmospheres, 113, https://doi.org/10.1029/2008JD009845, 2008.

Chen, G., Canonaco, F., Tobler, A., Aas, W., Alastuey, A., Allan, J., Atabakhsh, S., Aurela, M., Baltensperger, U., Bougiatioti, A., De Brito, J. F., Ceburnis, D., Chazeau, B., Chebaicheb, H., Daellenbach, K. R., Ehn, M., El Haddad, I., Eleftheriadis, K., Favez, O., Flentje, H., Font, A., Fossum, K., Freney, E., Gini, M., Green, D. C., Heikkinen, L., Herrmann, H., Kalogridis, A.-C., Keernik, H., Lhotka, R., Lin, C., Lunder, C., Maasikmets, M., Manousakas, M. I., Marchand, N., Marin, C., Marmureanu, L., Mihalopoulos, N., Močnik, G., Nęcki, J., O'Dowd, C., Ovadnevaite, J., Peter, T., Petit, J.-E., Pikridas, M., Matthew Platt, S., Pokorná, P., Poulain, L., Priestman, M., Riffault, V., Rinaldi, M., Różański, K., Schwarz, J., Sciare, J., Simon, L., Skiba, A., Slowik, J. G., Sosedova, Y., Stavroulas, I., Styszko, K., Teinemaa, E., Timonen, H., Tremper, A., Vasilescu, J., Via, M., Vodička, P., Wiedensohler, A., Zografou, O., Cruz Minguillón, M., and Prévôt, A. S. H.: European aerosol phenomenology − 8: Harmonised source apportionment of organic aerosol using 22 Year-long ACSM/AMS datasets, Environment International, 166, 107325, https://doi.org/10.1016/j.envint.2022.107325, 2022.

Chen, Y., Xu, L., Humphry, T., Hettiyadura, A. P. S., Ovadnevaite, J., Huang, S., Poulain, L., Schroder, J. C., Campuzano-Jost, P., Jimenez, J. L., Herrmann, H., O'Dowd, C., Stone, E. A., and Ng, N. L.: Response of the Aerodyne Aerosol Mass

Spectrometer to Inorganic Sulfates and Organosulfur Compounds: Applications in Field and Laboratory Measurements, Environmental Science & Technology, 53, 5176–5186, 10.1021/acs.est.9b00884, 2019.

Ciarelli, G., Theobald, M. R., Vivanco, M. G., Beekmann, M., Aas, W., Andersson, C., Bergström, R., Manders-Groot, A., Couvidat, F., Mircea, M., Tsyro, S., Fagerli, H., Mar, K., Raffort, V., Roustan, Y., Pay, M. T., Schaap, M., Kranenburg, R., Adani, M., Briganti, G., Cappelletti, A., D'Isidoro, M., Cuvelier, C., Cholakian, A., Bessagnet, B., Wind, P., and Colette, A.: Trends of inorganic and organic aerosols and precursor gases in Europe: insights from the EURODELTA multi-model experiment over the 1990–2010 period, Geosci. Model Dev., 12, 4923–4954, 10.5194/gmd-12-4923-2019, 2019.

Cirino, G., Brito, J., Barbosa, H. M. J., Rizzo, L. V., Tunved, P., de Sá, S. S., Jimenez, J. L., Palm, B. B., Carbone, S., Lavric, J. V., Souza, R. A. F., Wolff, S., Walter, D., Tota, J., Oliveira, M. B. L., Martin, S. T., and Artaxo, P.: Observations of Manaus urban plume evolution and interaction with biogenic emissions in GoAmazon 2014/5, Atmospheric Environment, 191, 513–524, https://doi.org/10.1016/j.atmosenv.2018.08.031, 2018.

Cross, E. S., Slowik, J. G., Davidovits, P., Allan, J. D., Worsnop, D. R., Jayne, J. T., Lewis †, D. K., Canagaratna, M., and Onasch, T. B.: Laboratory and Ambient Particle Density Determinations using Light Scattering in Conjunction with Aerosol Mass Spectrometry, Aerosol Science and Technology, 41, 343–359, 10.1080/02786820701199736, 2007.

Curci, G., Alyuz, U., Barò, R., Bianconi, R., Bieser, J., Christensen, J. H., Colette, A., Farrow, A., Francis, X., Jiménez-Guerrero, P., Im, U., Liu, P., Manders, A., Palacios-Peña, L., Prank, M., Pozzoli, L., Sokhi, R., Solazzo, E., Tuccella, P., Unal, A., Vivanco, M. G., Hogrefe, C., and Galmarini, S.: Modelling black carbon absorption of solar radiation: combining external and internal mixing assumptions, Atmos. Chem. Phys., 19, 181–204, 10.5194/acp-19-181-2019, 2019.

Davies, N. W., Fox, C., Szpek, K., Cotterell, M. I., Taylor, J. W., Allan, J. D., Williams, P. I., Trembath, J., Haywood, J. M., and Langridge, J. M.: Evaluating biases in filter-based aerosol absorption measurements using photoacoustic spectroscopy, Atmos. Meas. Tech., 12, 3417–3434, 10.5194/amt-12-3417-2019, 2019.

DeCarlo, P. F., Ulbrich, I. M., Crounse, J., de Foy, B., Dunlea, E. J., Aiken, A. C., Knapp, D., Weinheimer, A. J., Campos, T., Wennberg, P. O., and Jimenez, J. L.: Investigation of the sources and processing of organic aerosol over the Central Mexican Plateau from aircraft measurements during MILAGRO, Atmos. Chem. Phys., 10, 5257–5280, 10.5194/acp-10-5257-2010, 2010.

DeCarlo, P. F., Dunlea, E. J., Kimmel, J. R., Aiken, A. C., Sueper, D., Crounse, J., Wennberg, P. O., Emmons, L., Shinozuka, Y., Clarke, A., Zhou, J., Tomlinson, J., Collins, D. R., Knapp, D., Weinheimer, A. J., Montzka, D. D., Campos, T., and Jimenez, J. L.: Fast airborne aerosol size and chemistry measurements above Mexico City and Central Mexico during the MILAGRO campaign, Atmos. Chem. Phys., 8, 4027–4048, 10.5194/acp-8-4027-2008, 2008.

Di Antonio, L., Di Biagio, C., Formenti, P., Gratien, A., Michoud, V., Cantrell, C., Bauville, A., Bergé, A., Cazaunau, M., Chevaillier, S., Cirtog, M., Coll, P., D'Anna, B., de Brito, J. F., De Haan, D. O., Dignum, J. R., Deshmukh, S., Favez, O., Flaud, P. M., Gaimoz, C., Hawkins, L. N., Kammer, J., Language, B., Maisonneuve, F., Močnik, G., Perraudin, E., Petit, J. E., Acharja, P., Poulain, L., Pouyes, P., Pronovost, E. D., Riffault, V., Roundtree, K. I., Shahin, M., Siour, G., Villenave, E., Zapf, P., Foret, G., Doussin, J. F., and Beekmann, M.: Aerosol spectral optical properties in the Paris urban area and its peri-urban and forested surroundings during summer 2022 from ACROSS surface observations, Atmos. Chem. Phys., 25, 3161–3189, 10.5194/acp-25-3161-2025, 2025.

Di Carlo, P., Aruffo, E., Busilacchio, M., Giammaria, F., Dari-Salisburgo, C., Biancofiore, F., Visconti, G., Lee, J., Moller, S., Reeves, C. E., Bauguitte, S., Forster, G., Jones, R. L., and Ouyang, B.: Aircraft based four-channel thermal dissociation laser induced fluorescence instrument for simultaneous measurements of NO₂, total peroxy nitrate, total alkyl nitrate, and HNO₃, Atmos. Meas. Tech., 6, 971–980, 10.5194/amt-6-971-2013, 2013.

Dingle, J. H., Vu, K., Bahreini, R., Apel, E. C., Campos, T. L., Flocke, F., Fried, A., Herndon, S., Hills, A. J., Hornbrook, R. S., Huey, G., Kaser, L., Montzka, D. D., Nowak, J. B., Reeves, M., Richter, D., Roscioli, J. R., Shertz, S., Stell, M., Tanner, D., Tyndall, G., Walega, J., Weibring, P., and Weinheimer, A.: Aerosol optical extinction during the Front Range Air Pollution and Photochemistry Éxperiment (FRAPPÉ) 2014 summertime field campaign, Colorado, USA, Atmos. Chem. Phys., 16, 11207–11217, 10.5194/acp-16-11207-2016, 2016.

Drewnick, F., Hings, S. S., DeCarlo, P., Jayne, J. T., Gonin, M., Fuhrer, K., Weimer, S., Jimenez, J. L., Demerjian, K. L., Borrmann, S., and Worsnop, D. R.: A New Time-of-Flight Aerosol Mass Spectrometer (TOF-AMS)—Instrument Description and First Field Deployment, Aerosol Science and Technology, 39, 637–658, 10.1080/02786820500182040, 2005.

Drugé, T., Nabat, P., Mallet, M., Michou, M., Rémy, S., and Dubovik, O.: Modeling radiative and climatic effects of brown carbon aerosols with the ARPEGE-Climat global climate model, Atmos. Chem. Phys., 22, 12167–12205, 10.5194/acp-22-12167-2022, 2022.

Eom, S., Park, S. S., Liu, X., Oxford, C. R., Martin, R. V., Kim, J., and Song, C.-K.: Impact of Chemical Composition on Aerosol Scattering: Insights from the Surface Particulate Matter Network and Aerosol Robotic Network, Environmental Science & Technology, 59, 19899–19909, 10.1021/acs.est.5c09325, 2025.

Farmer, D. K., Cappa, C. D., and Kreidenweis, S. M.: Atmospheric Processes and Their Controlling Influence on Cloud Condensation Nuclei Activity, Chemical Reviews, 115, 4199–4217, 10.1021/cr5006292, 2015.

Farmer, D. K., Matsunaga, A., Docherty, K. S., Surratt, J. D., Seinfeld, J. H., Ziemann, P. J., and Jimenez, J. L.: Response of an aerosol mass spectrometer to organonitrates and organosulfates and implications for atmospheric chemistry, Proceedings of the National Academy of Sciences, 107, 6670–6675, 10.1073/pnas.0912340107, 2010.

Flores, J. M., Zhao, D. F., Segev, L., Schlag, P., Kiendler-Scharr, A., Fuchs, H., Watne, Å. K., Bluvshtein, N., Mentel, T. F., Hallquist, M., and Rudich, Y.: Evolution of the complex refractive index in the UV spectral region in ageing secondary organic aerosol, Atmos. Chem. Phys., 14, 5793–5806, 10.5194/acp-14-5793-2014, 2014.

Flowers, B. A., Dubey, M. K., Mazzoleni, C., Stone, E. A., Schauer, J. J., Kim, S. W., and Yoon, S. C.: Optical-chemical-microphysical relationships and closure studies for mixed carbonaceous aerosols observed at Jeju Island; 3-laser photoacoustic spectrometer, particle sizing, and filter analysis, Atmos. Chem. Phys., 10, 10387–10398, 10.5194/acp-10-10387-2010, 2010.

Formenti, P., Rajot, J. L., Desboeufs, K., Saïd, F., Grand, N., Chevaillier, S., and Schmechtig, C.: Airborne observations of mineral dust over western Africa in the summer Monsoon season: spatial and vertical variability of physico-chemical and optical properties, Atmos. Chem. Phys., 11, 6387–6410, 10.5194/acp-11-6387-2011, 2011.

Freney, E. J., Sellegri, K., Canonaco, F., Colomb, A., Borbon, A., Michoud, V., Doussin, J. F., Crumeyrolle, S., Amarouche, N., Pichon, J. M., Bourianne, T., Gomes, L., Prevot, A. S. H., Beekmann, M., and Schwarzenböeck, A.: Characterizing the impact of urban emissions on regional aerosol particles: airborne measurements during the MEGAPOLI experiment, Atmos. Chem. Phys., 14, 1397–1412, 10.5194/acp-14-1397-2014, 2014.

Fröhlich, R., Cubison, M. J., Slowik, J. G., Bukowiecki, N., Prévôt, A. S. H., Baltensperger, U., Schneider, J., Kimmel, J. R., Gonin, M., Rohner, U., Worsnop, D. R., and Jayne, J. T.: The ToF-ACSM: a portable aerosol chemical speciation monitor with TOFMS detection, Atmos. Meas. Tech., 6, 3225–3241, 10.5194/amt-6-3225-2013, 2013.

Goetz, J. D., Giordano, M. R., Stockwell, C. E., Bhave, P. V., Puppala, P. S., Panday, A. K., Jayarathne, T., Stone, E. A., Yokelson, R. J., and DeCarlo, P. F.: Aerosol Mass Spectral Profiles from NAMaSTE Field-Sampled South Asian Combustion Sources, ACS Earth and Space Chemistry, 6, 2619–2631, 10.1021/acsearthspacechem.2c00173, 2022.

Goetz, J. D., Giordano, M. R., Stockwell, C. E., Christian, T. J., Maharjan, R., Adhikari, S., Bhave, P. V., Praveen, P. S., Panday, A. K., Jayarathne, T., Stone, E. A., Yokelson, R. J., and DeCarlo, P. F.: Speciated online PM1 from South Asian combustion sources – Part 1: Fuel-based emission factors and size distributions, Atmos. Chem. Phys., 18, 14653–14679, 10.5194/acp-18-14653-2018, 2018.

Grange, S. K., Lee, J. D., Drysdale, W. S., Lewis, A. C., Hueglin, C., Emmenegger, L., and Carslaw, D. C.: COVID-19 lockdowns highlight a risk of increasing ozone pollution in European urban areas, Atmos. Chem. Phys., 21, 4169–4185, 10.5194/acp-21-4169-2021, 2021.

Grzegorski, M., Poli, G., Cacciari, A., Jafariserajehlou, S., Holdak, A., Lang, R., Vazquez-Navarro, M., Munro, R., and Fougnie, B.: Multi-Sensor Retrieval of Aerosol Optical Properties for Near-Real-Time Applications Using the Metop Series of Satellites: Concept, Detailed Description, and First Validation, 10.3390/rs14010085, 2022.

Harrison, R. M., Beddows, D. C. S., Alam, M. S., Singh, A., Brean, J., Xu, R., Kotthaus, S., and Grimmond, S.: Interpretation of particle number size distributions measured across an urban area during the FASTER campaign, Atmos. Chem. Phys., 19, 39–55, 10.5194/acp-19-39-2019, 2019.

Hayes, P. L., Ortega, A. M., Cubison, M. J., Froyd, K. D., Zhao, Y., Cliff, S. S., Hu, W. W., Toohey, D. W., Flynn, J. H., Lefer, B. L., Grossberg, N., Alvarez, S., Rappenglück, B., Taylor, J. W., Allan, J. D., Holloway, J. S., Gilman, J. B., Kuster, W. C., de Gouw, J. A., Massoli, P., Zhang, X., Liu, J., Weber, R. J., Corrigan, A. L., Russell, L. M., Isaacman, G., Worton, D. R., Kreisberg, N. M., Goldstein, A. H., Thalman, R., Waxman, E. M., Volkamer, R., Lin, Y. H., Surratt, J. D., Kleindienst, T. E., Offenberg, J. H., Dusanter, S., Griffith, S., Stevens, P. S., Brioude, J., Angevine, W. M., and Jimenez, J. L.: Organic aerosol composition and sources in Pasadena, California, during the 2010 CalNex campaign, Journal of Geophysical Research: Atmospheres, 118, 9233–9257, https://doi.org/10.1002/jgrd.50530, 2013.

He, Q., Tomaz, S., Li, C., Zhu, M., Meidan, D., Riva, M., Laskin, A., Brown, S. S., George, C., Wang, X., and Rudich, Y.: Optical Properties of Secondary Organic Aerosol Produced by Nitrate Radical Oxidation of Biogenic Volatile Organic Compounds, Environmental Science & Technology, 55, 2878–2889, 10.1021/acs.est.0c06838, 2021.

Herrera, M. E., Dubovik, O., Torres, B., Lapyonok, T., Fuertes, D., Lopatin, A., Litvinov, P., Chen, C., Benavent-Oltra, J. A., Bali, J. L., and Ristori, P. R.: Estimates of remote sensing retrieval errors by the GRASP algorithm: application to ground-based observations, concept and validation, Atmospheric Measurement Techniques, 15, 6075–6126, 10.5194/amt-15-6075-2022, 2022.

Jathar, S. H., Woody, M., Pye, H. O. T., Baker, K. R., and Robinson, A. L.: Chemical transport model simulations of organic aerosol in southern California: model evaluation and gasoline and diesel source contributions, Atmos. Chem. Phys., 17, 4305–4318, 10.5194/acp-17-4305-2017, 2017.

Jiang, X., Xue, Y., de Leeuw, G., Jin, C., Zhang, S., Sun, Y., and Wu, S.: Retrieval of hourly aerosol single scattering albedo over land using geostationary satellite data, npj Climate and Atmospheric Science, 7, 157, 10.1038/s41612-024-00690-6, 2024.

Jimenez, J. L., Canagaratna, M. R., Donahue, N. M., Prevot, A. S. H., Zhang, Q., Kroll, J. H., DeCarlo, P. F., Allan, J. D., Coe, H., Ng, N. L., Aiken, A. C., Docherty, K. S., Ulbrich, I. M., Grieshop, A. P., Robinson, A. L., Duplissy, J., Smith, J. D., Wilson, K. R., Lanz, V. A., Hueglin, C., Sun, Y. L., Tian, J., Laaksonen, A., Raatikainen, T., Rautiainen, J., Vaattovaara, P., Ehn, M., Kulmala, M., Tomlinson, J. M., Collins, D. R., Cubison, M. J., E, Dunlea, J., Huffman, J. A., Onasch, T. B., Alfarra, M. R., Williams, P. I., Bower, K., Kondo, Y., Schneider, J., Drewnick, F., Borrmann, S., Weimer, S., Demerjian, K., Salcedo, D., Cottrell, L., Griffin, R., Takami, A., Miyoshi, T., Hatakeyama, S., Shimono, A., Sun, J. Y., Zhang, Y. M., Dzepina, K., Kimmel, J. R., Sueper, D., Jayne, J. T., Herndon, S. C., Trimborn, A. M., Williams, L. R., Wood, E. C., Middlebrook, A. M., Kolb, C. E., Baltensperger, U., and Worsnop, D. R.: Evolution of Organic Aerosols in the Atmosphere, Science, 326, 1525–1529, 10.1126/science.1180353, 2009.

Jones, A., Thomson, D., Hort, M., and Devenish, B.: The U.K. Met Office's Next-Generation Atmospheric Dispersion Model, NAME III, Air Pollution Modeling and Its Application XVII, Boston, MA, 2007//, 580–589,

Kahn, R. A., Andrews, E., Brock, C. A., Chin, M., Feingold, G., Gettelman, A., Levy, R. C., Murphy, D. M., Nenes, A., Pierce, J. R., Popp, T., Redemann, J., Sayer, A. M., da Silva, A. M., Sogacheva, L., and Stier, P.: Reducing Aerosol Forcing Uncertainty by Combining Models With Satellite and Within-The-Atmosphere Observations: A Three-Way Street, Reviews of Geophysics, 61, e2022RG000796, https://doi.org/10.1029/2022RG000796, 2023.

Karagulian, F., Belis, C. A., Dora, C. F. C., Prüss-Ustün, A. M., Bonjour, S., Adair-Rohani, H., and Amann, M.: Contributions to cities' ambient particulate matter (PM): A systematic review of local source contributions at global level, Atmospheric Environment, 120, 475–483, https://doi.org/10.1016/j.atmosenv.2015.08.087, 2015.

Konovalov, I. B., Golovushkin, N. A., Beekmann, M., and Andreae, M. O.: Insights into the aging of biomass burning aerosol from satellite observations and 3D atmospheric modeling: evolution of the aerosol optical properties in Siberian wildfire plumes, Atmos. Chem. Phys., 21, 357–392, 10.5194/acp-21-357-2021, 2021.

Konwar, M., Werden, B., Fortner, E. C., Bera, S., Varghese, M., Chowdhuri, S., Hibert, K., Croteau, P., Jayne, J., Canagaratna, M., Malap, N., Jayakumar, S., Dixit, S. A., Murugavel, P., Axisa, D., Baumgardner, D., DeCarlo, P. F., Worsnop, D. R., and Prabhakaran, T.: Identifying the seeding signature in cloud particles from hydrometeor residuals, Atmos. Meas. Tech., 17, 2387–2400, 10.5194/amt-17-2387-2024, 2024.

Laing, J. R., Jaffe, D. A., and Sedlacek, I. I. I. A. J.: Comparison of Filter-based Absorption Measurements of Biomass Burning Aerosol and Background Aerosol at the Mt. Bachelor Observatory, Aerosol and Air Quality Research, 20, 663–678, 10.4209/aaqr.2019.06.0298, 2020.

Langridge, J. M., Lack, D., Brock, C. A., Bahreini, R., Middlebrook, A. M., Neuman, J. A., Nowak, J. B., Perring, A. E., Schwarz, J. P., Spackman, J. R., Holloway, J. S., Pollack, I. B., Ryerson, T. B., Roberts, J. M., Warneke, C., de Gouw, J. A., Trainer, M. K., and Murphy, D. M.: Evolution of aerosol properties impacting visibility and direct climate forcing in an ammonia-rich urban environment, Journal of Geophysical Research: Atmospheres, 117, https://doi.org/10.1029/2011JD017116, 2012.

Levy, R. C., Remer, L. A., and Dubovik, O.: Global aerosol optical properties and application to Moderate Resolution Imaging Spectroradiometer aerosol retrieval over land, Journal of Geophysical Research: Atmospheres, 112, https://doi.org/10.1029/2006JD007815, 2007.

Li, C., van Donkelaar, A., Hammer, M. S., McDuffie, E. E., Burnett, R. T., Spadaro, J. V., Chatterjee, D., Cohen, A. J., Apte, J. S., Southerland, V. A., Anenberg, S. C., Brauer, M., and Martin, R. V.: Reversal of trends in global fine particulate matter air pollution, Nature Communications, 14, 5349, 10.1038/s41467-023-41086-z, 2023.

Li, H., Zhang, Q., Zheng, B., Chen, C., Wu, N., Guo, H., Zhang, Y., Zheng, Y., Li, X., and He, K.: Nitrate-driven urban haze pollution during summertime over the North China Plain, Atmos. Chem. Phys., 18, 5293–5306, 10.5194/acp-18-5293-2018, 2018.

Li, J., Carlson, B. E., Yung, Y. L., Lv, D., Hansen, J., Penner, J. E., Liao, H., Ramaswamy, V., Kahn, R. A., Zhang, P., Dubovik, O., Ding, A., Lacis, A. A., Zhang, L., and Dong, Y.: Scattering and absorbing aerosols in the climate system, Nature Reviews Earth & Environment, 3, 363–379, 10.1038/s43017-022-00296-7, 2022a.

Li, L., Derimian, Y., Chen, C., Zhang, X., Che, H., Schuster, G. L., Fuertes, D., Litvinov, P., Lapyonok, T., Lopatin, A., Matar, C., Ducos, F., Karol, Y., Torres, B., Gui, K., Zheng, Y., Liang, Y., Lei, Y., Zhu, J., Zhang, L., Zhong, J., Zhang, X., and Dubovik, O.: Climatology of aerosol component concentrations derived from multi-angular polarimetric POLDER-3 observations using GRASP algorithm, Earth Syst. Sci. Data, 14, 3439–3469, 10.5194/essd-14-3439-2022, 2022b.

Manisalidis, I., Stavropoulou, E., Stavropoulos, A., and Bezirtzoglou, E.: Environmental and Health Impacts of Air Pollution: A Review, Front Public Health, 8, 14, 10.3389/fpubh.2020.00014, 2020.

McMeeking, G. R., Bart, M., Chazette, P., Haywood, J. M., Hopkins, J. R., McQuaid, J. B., Morgan, W. T., Raut, J. C., Ryder, C. L., Savage, N., Turnbull, K., and Coe, H.: Airborne measurements of trace gases and aerosols over the London metropolitan region, Atmos. Chem. Phys., 12, 5163–5187, 10.5194/acp-12-5163-2012, 2012.

Morgan, W. T., Allan, J. D., Bower, K. N., Highwood, E. J., Liu, D., McMeeking, G. R., Northway, M. J., Williams, P. I., Krejci, R., and Coe, H.: Airborne measurements of the spatial distribution of aerosol chemical composition across Europe and evolution of the organic fraction, Atmos. Chem. Phys., 10, 4065–4083, 10.5194/acp-10-4065-2010, 2010.

Nault, B. A., Campuzano-Jost, P., Day, D. A., Schroder, J. C., Anderson, B., Beyersdorf, A. J., Blake, D. R., Brune, W. H., Choi, Y., Corr, C. A., de Gouw, J. A., Dibb, J., DiGangi, J. P., Diskin, G. S., Fried, A., Huey, L. G., Kim, M. J., Knote, C. J., Lamb, K. D., Lee, T., Park, T., Pusede, S. E., Scheuer, E., Thornhill, K. L., Woo, J. H., and Jimenez, J. L.: Secondary organic aerosol production from local emissions dominates the organic aerosol budget over Seoul, South Korea, during KORUS-AQ, Atmos. Chem. Phys., 18, 17769–17800, 10.5194/acp-18-17769-2018, 2018.

Nault, B. A., Jo, D. S., McDonald, B. C., Campuzano-Jost, P., Day, D. A., Hu, W., Schroder, J. C., Allan, J., Blake, D. R., Canagaratna, M. R., Coe, H., Coggon, M. M., DeCarlo, P. F., Diskin, G. S., Dunmore, R., Flocke, F., Fried, A., Gilman, J. B., Gkatzelis, G., Hamilton, J. F., Hanisco, T. F., Hayes, P. L., Henze, D. K., Hodzic, A., Hopkins, J., Hu, M., Huey, L. G., Jobson, B. T., Kuster, W. C., Lewis, A., Li, M., Liao, J., Nawaz, M. O., Pollack, I. B., Peischl, J., Rappenglück, B., Reeves, C. E., Richter, D., Roberts, J. M., Ryerson, T. B., Shao, M., Sommers, J. M., Walega, J., Warneke, C., Weibring, P., Wolfe, G. M., Young, D. E., Yuan, B., Zhang, Q., de Gouw, J. A., and Jimenez, J. L.: Secondary organic aerosols from anthropogenic volatile organic compounds contribute substantially to air pollution mortality, Atmos. Chem. Phys., 21, 11201–11224, 10.5194/acp-21-11201-2021, 2021.

Onasch, T. B., Massoli, P., Kebabian, P. L., Hills, F. B., Bacon, F. W., and Freedman, A.: Single Scattering Albedo Monitor for Airborne Particulates, Aerosol Science and Technology, 49, 267–279, 10.1080/02786826.2015.1022248, 2015.

Pereira, D. L., Giorio, C., Gratien, A., Zherebker, A., Noyalet, G., Chevaillier, S., Alage, S., Almarj, E., Bergé, A., Bertin, T., Cazaunau, M., Coll, P., Di Antonio, L., Harb, S., Heuser, J., Gaimoz, C., Guillemant, O., Language, B., Lauret, O., Macias, C., Maisonneuve, F., Picquet-Varrault, B., Torres, R., Triquet, S., Zapf, P., Hawkins, L., Pronovost, D., Riley, S., Flaud, P. M., Perraudin, E., Pouyes, P., Villenave, E., Albinet, A., Favez, O., Aujay-Plouzeau, R., Michoud, V., Cantrell, C., Cirtog, M., Di Biagio, C., Doussin, J. F., and Formenti, P.: Molecular characterization of organic aerosols in urban and forested areas of Paris using high-resolution mass spectrometry, Atmos. Chem. Phys., 25, 4885–4905, 10.5194/acp-25-4885-2025, 2025.

Petzold, A., Ogren, J. A., Fiebig, M., Laj, P., Li, S. M., Baltensperger, U., Holzer-Popp, T., Kinne, S., Pappalardo, G., Sugimoto, N., Wehrli, C., Wiedensohler, A., and Zhang, X. Y.: Recommendations for reporting "black carbon" measurements, Atmos. Chem. Phys., 13, 8365–8379, 10.5194/acp-13-8365-2013, 2013.

Pieber, S. M., El Haddad, I., Slowik, J. G., Canagaratna, M. R., Jayne, J. T., Platt, S. M., Bozzetti, C., Daellenbach, K. R., Fröhlich, R., Vlachou, A., Klein, F., Dommen, J., Miljevic, B., Jiménez, J. L., Worsnop, D. R., Baltensperger, U., and Prévôt, A. S. H.: Inorganic Salt Interference on CO2+ in Aerodyne AMS and ACSM Organic Aerosol Composition Studies, Environmental Science & Technology, 50, 10494–10503, 10.1021/acs.est.6b01035, 2016.

Raut, J. C. and Chazette, P.: Vertical profiles of urban aerosol complex refractive index in the frame of ESQUIF airborne measurements, Atmos. Chem. Phys., 8, 901–919, 10.5194/acp-8-901-2008, 2008.

Ravishankara, A. R., Rudich, Y., and Wuebbles, D. J.: Physical Chemistry of Climate Metrics, Chemical Reviews, 115, 3682–3703, 10.1021/acs.chemrev.5b00010, 2015.

Riemer, N., Ault, A. P., West, M., Craig, R. L., and Curtis, J. H.: Aerosol Mixing State: Measurements, Modeling, and Impacts, Reviews of Geophysics, 57, 187–249, https://doi.org/10.1029/2018RG000615, 2019.

Savadkoohi, M., Pandolfi, M., Reche, C., Niemi, J. V., Mooibroek, D., Titos, G., Green, D. C., Tremper, A. H., Hueglin, C., Liakakou, E., Mihalopoulos, N., Stavroulas, I., Artiñano, B., Coz, E., Alados-Arboledas, L., Beddows, D., Riffault, V., De Brito, J. F., Bastian, S., Baudic, A., Colombi, C., Costabile, F., Chazeau, B., Marchand, N., Gómez-Amo, J. L., Estellés, V., Matos, V., van der Gaag, E., Gille, G., Luoma, K., Manninen, H. E., Norman, M., Silvergren, S., Petit, J.-E., Putaud, J.-P., Rattigan, O. V., Timonen, H., Tuch, T., Merkel, M., Weinhold, K., Vratolis, S., Vasilescu, J., Favez, O., Harrison, R. M., Laj, P., Wiedensohler, A., Hopke, P. K., Petäjä, T., Alastuey, A., and Querol, X.: The variability of mass concentrations and source apportionment analysis of equivalent black carbon across urban Europe, Environment International, 178, 108081, https://doi.org/10.1016/j.envint.2023.108081, 2023.

Schroder, J. C., Campuzano-Jost, P., Day, D. A., Shah, V., Larson, K., Sommers, J. M., Sullivan, A. P., Campos, T., Reeves, J. M., Hills, A., Hornbrook, R. S., Blake, N. J., Scheuer, E., Guo, H., Fibiger, D. L., McDuffie, E. E., Hayes, P. L., Weber, R. J., Dibb, J. E., Apel, E. C., Jaeglé, L., Brown, S. S., Thornton, J. A., and Jimenez, J. L.: Sources and Secondary Production of Organic Aerosols in the Northeastern United States during WINTER, Journal of Geophysical Research: Atmospheres, 123, 7771–7796, https://doi.org/10.1029/2018JD028475, 2018.

Shen, J., Kuang, Y., Liu, L., Yuan, F., Luo, B., Qiao, H., Zhai, M., Zhao, G., Xu, H., Li, F., Zou, Y., Deng, T., and Deng, X.: Refractive index enhancement by secondary organic aerosol formation in humid southern China challenges model assumptions, Atmos. Chem. Phys., 25, 11233–11246, 10.5194/acp-25-11233-2025, 2025.

Shepherd, R. H., King, M. D., Marks, A. A., Brough, N., and Ward, A. D.: Determination of the refractive index of insoluble organic extracts from atmospheric aerosol over the visible wavelength range using optical tweezers, Atmos. Chem. Phys., 18, 5235–5252, 10.5194/acp-18-5235-2018, 2018.

Shilling, J. E., Pekour, M. S., Fortner, E. C., Artaxo, P., de Sá, S., Hubbe, J. M., Longo, K. M., Machado, L. A. T., Martin, S. T., Springston, S. R., Tomlinson, J., and Wang, J.: Aircraft observations of the chemical composition and aging of aerosol in the Manaus urban plume during GoAmazon 2014/5, Atmos. Chem. Phys., 18, 10773–10797, 10.5194/acp-18-10773-2018, 2018.

Shingler, T., Crosbie, E., Ortega, A., Shiraiwa, M., Zuend, A., Beyersdorf, A., Ziemba, L., Anderson, B., Thornhill, L., Perring, A. E., Schwarz, J. P., Campazano-Jost, P., Day, D. A., Jimenez, J. L., Hair, J. W., Mikoviny, T., Wisthaler, A., and Sorooshian, A.: Airborne characterization of subsaturated aerosol hygroscopicity and dry refractive index from the surface to 6.5 km during the SEAC4RS campaign, Journal of Geophysical Research: Atmospheres, 121, 4188–4210, https://doi.org/10.1002/2015JD024498, 2016.

Taylor, J. W., Allan, J. D., Liu, D., Flynn, M., Weber, R., Zhang, X., Lefer, B. L., Grossberg, N., Flynn, J., and Coe, H.: Assessment of the sensitivity of core / shell parameters derived using the single-particle soot photometer to density and refractive index, Atmos. Meas. Tech., 8, 1701–1718, 10.5194/amt-8-1701-2015, 2015.

Teri, M., Müller, T., Gasteiger, J., Valentini, S., Horvath, H., Vecchi, R., Bauer, P., Walser, A., and Weinzierl, B.: Impact of particle size, refractive index, and shape on the determination of the particle scattering coefficient – an optical closure study evaluating different nephelometer angular truncation and illumination corrections, Atmospheric Measurement Techniques, 15, 3161–3187, 10.5194/amt-15-3161-2022, 2022.

Tian, P., Liu, D., Zhao, D., Yu, C., Liu, Q., Huang, M., Deng, Z., Ran, L., Wu, Y., Ding, S., Hu, K., Zhao, G., Zhao, C., and Ding, D.: In situ vertical characteristics of optical properties and heating rates of aerosol over Beijing, Atmos. Chem. Phys., 20, 2603–2622, 10.5194/acp-20-2603-2020, 2020.

Tinorua, S., Denjean, C., Nabat, P., Bourrianne, T., Pont, V., Gheusi, F., and Leclerc, E.: Higher absorption enhancement of black carbon in summer shown by 2-year measurements at the high-altitude mountain site of Pic du Midi Observatory in the French Pyrenees, Atmos. Chem. Phys., 24, 1801–1824, 10.5194/acp-24-1801-2024, 2024a.

Tinorua, S., Denjean, C., Nabat, P., Pont, V., Arnaud, M., Bourrianne, T., Dias Alves, M., and Gardrat, E.: A 2-year intercomparison of three methods for measuring black carbon concentration at a high-altitude research station in Europe, Atmos. Meas. Tech., 17, 3897–3915, 10.5194/amt-17-3897-2024, 2024b.

Tsigaridis, K. and Kanakidou, M.: The Present and Future of Secondary Organic Aerosol Direct Forcing on Climate, Current Climate Change Reports, 4, 84–98, 10.1007/s40641-018-0092-3, 2018.

Tsigaridis, K., Daskalakis, N., Kanakidou, M., Adams, P. J., Artaxo, P., Bahadur, R., Balkanski, Y., Bauer, S. E., Bellouin, N., Benedetti, A., Bergman, T., Berntsen, T. K., Beukes, J. P., Bian, H., Carslaw, K. S., Chin, M., Curci, G., Diehl, T., Easter, R. C., Ghan, S. J., Gong, S. L., Hodzic, A., Hoyle, C. R., Iversen, T., Jathar, S., Jimenez, J. L., Kaiser, J. W., Kirkevåg, A., Koch, D., Kokkola, H., Lee, Y. H., Lin, G., Liu, X., Luo, G., Ma, X., Mann, G. W., Mihalopoulos, N., Morcrette, J. J., Müller, J. F., Myhre, G., Myriokefalitakis, S., Ng, N. L., O'Donnell, D., Penner, J. E., Pozzoli, L., Pringle, K. J., Russell, L. M., Schulz, M., Sciare, J., Seland, Ø., Shindell, D. T., Sillman, S., Skeie, R. B., Spracklen, D., Stavrakou, T., Steenrod, S. D., Takemura, T., Tiitta, P., Tilmes, S., Tost, H., van Noije, T., van Zyl, P. G., von Salzen, K., Yu, F., Wang, Z., Wang, Z., Zaveri, R. A., Zhang, H., Zhang, K., Zhang, Q., and Zhang, X.: The AeroCom evaluation and intercomparison of organic aerosol in global models, Atmos. Chem. Phys., 14, 10845–10895, 10.5194/acp-14-10845-2014, 2014.

Tsimpidi, A. P., Scholz, S. M. C., Milousis, A., Mihalopoulos, N., and Karydis, V. A.: Aerosol composition trends during 2000–2020: in-depth insights from model predictions and multiple worldwide near-surface observation datasets, Atmos. Chem. Phys., 25, 10183–10213, 10.5194/acp-25-10183-2025, 2025.

Velazquez-Garcia, A., Denjean, C., Yu, C., Tinorua, S., Bourrianne, T., Burnet, F., Tu, K., Pangui, E., Pereira, D. L., Cazaunau, M., Di Antonio, L., Siour, G., Beekmann, M., DeCarlo, P. F., Nault, B. A., Bauville, A., Cantrell, C., Formenti, P., and Michoud, V.: Observational Evidence for Relative Humidity Driving Black Carbon Mixing State and Absorption Enhancement in Urban Outflows, Geophysical Research Letters, 53, e2025GL121520, https://doi.org/10.1029/2025GL121520, 2026a.

Velazquez-Garcia, A., Yu, C., Tinorua, S., Bouzidi, H., Aruffo, E., Di Carlo, P., DeCarlo, P., A. Nault, B., Bourrianne, T., Tu, K., Pangui, E., L. Pereira, D., Cazaunau, M., Di Antonio, L., Siour, G., Beekmann, M., Bauville, A., Cantrell, C., Formenti, P., Michoud, V., and Denjean, C.: Photochemical ageing drives the browning of urban outflows through secondary brown carbon production, EGUsphere, 2026, 1–28, 10.5194/egusphere-2026-4423, 2026b.

von der Weiden, S. L., Drewnick, F., and Borrmann, S.: Particle Loss Calculator – a new software tool for the assessment of the performance of aerosol inlet systems, Atmos. Meas. Tech., 2, 479–494, 10.5194/amt-2-479-2009, 2009.

Vu, K. T., Dingle, J. H., Bahreini, R., Reddy, P. J., Apel, E. C., Campos, T. L., DiGangi, J. P., Diskin, G. S., Fried, A., Herndon, S. C., Hills, A. J., Hornbrook, R. S., Huey, G., Kaser, L., Montzka, D. D., Nowak, J. B., Pusede, S. E., Richter, D., Roscioli, J. R., Sachse, G. W., Shertz, S., Stell, M., Tanner, D., Tyndall, G. S., Walega, J., Weibring, P., Weinheimer, A. J., Pfister, G., and Flocke, F.: Impacts of the Denver Cyclone on regional air quality and aerosol formation in the Colorado Front Range during FRAPPÉ 2014, Atmos. Chem. Phys., 16, 12039–12058, 10.5194/acp-16-12039-2016, 2016.

Weber, P., Petzold, A., Bischof, O. F., Fischer, B., Berg, M., Freedman, A., Onasch, T. B., and Bundke, U.: Relative errors in derived multi-wavelength intensive aerosol optical properties using cavity attenuated phase shift single-scattering albedo monitors, a nephelometer, and tricolour absorption photometer measurements, Atmos. Meas. Tech., 15, 3279–3296, 10.5194/amt-15-3279-2022, 2022.

Werden, B. S., Giordano, M. R., Mahata, K., Islam, M. R., Goetz, J. D., Puppala, S. P., Saikawa, E., Panday, A. K., Yokelson, R. J., Stone, E. A., and DeCarlo, P. F.: Submicron Aerosol Composition and Source Contribution across the Kathmandu Valley, Nepal, in Winter, ACS Earth and Space Chemistry, 7, 49–68, 10.1021/acsearthspacechem.2c00226, 2023.

Wu, Y., Li, J., Xia, Y., Deng, Z., Tao, J., Tian, P., Gao, Z., Xia, X., and Zhang, R.: Size-resolved refractive index of scattering aerosols in urban Beijing: A seasonal comparison, Aerosol Science and Technology, 55, 1070–1083, 10.1080/02786826.2021.1924357, 2021.

Xu, L., Lin, G., Wu, C., Chen, X., Wang, H., Chen, C., Chakrabarty, R. K., Gao, M., Vakkari, V., van Zyl, P. G., and Liu, X.: Strong global radiative effects from wildfire dark brown carbon, Nature Geoscience, 19, 612–619, 10.1038/s41561-026-01972-9, 2026.

Yu, C., Pangui, E., Tu, K., Cazaunau, M., Feingesicht, M., Xavier, L., Bourrianne, T., Michoud, V., Cantrell, C., Onasch, T. B., Freedman, A., and Formenti, P.: Characterisation of particle single-scattering albedo with a modified airborne dual-wavelength CAPS monitor, Atmospheric Measurement Techniques, 17, 3419–3437, 10.5194/amt-17-3419-2024, 2024.

Yu, C., Pasternak, D., Lee, J., Yang, M., Bell, T., Bower, K., Wu, H., Liu, D., Reed, C., Bauguitte, S., Cliff, S., Trembath, J., Coe, H., and Allan, J. D.: Characterizing the Particle Composition and Cloud Condensation Nuclei from Shipping Emission in Western Europe, Environmental Science & Technology, 54, 15604–15612, 10.1021/acs.est.0c04039, 2020.

Yu, C., Formenti, P., de Brito, J. F., Bauville, A., Bergé, A., Bouzidi, H., Cazaunau, M., Cirtog, M., Di Biagio, C., Di Antonio, L., Gaimoz, C., Maisonneuve, F., Zapf, P., Seubert, T., Andersen, S. T., Dewald, P., Türk, G. N. T. E., Crowley, J. N., Kukui,

A., Xue, C., Denjean, C., Garrouste, O., Etienne, J. C., Wu, H., Allan, J. D., Liu, D., Wu, Y., Cantrell, C., and Michoud, V.: Impacts of summertime photochemical aging on the physicochemical properties of aerosols in a Paris suburban forest region, EGUsphere, 2025, 1–28, 10.5194/egusphere-2025-2667, 2025.

Yus-Díez, J., Bernardoni, V., Močnik, G., Alastuey, A., Ciniglia, D., Ivančič, M., Querol, X., Perez, N., Reche, C., Rigler, M., Vecchi, R., Valentini, S., and Pandolfi, M.: Determination of the multiple-scattering correction factor and its cross-sensitivity to scattering and wavelength dependence for different AE33 Aethalometer filter tapes: a multi-instrumental approach, Atmos. Meas. Tech., 14, 6335–6355, 10.5194/amt-14-6335-2021, 2021.

Zaveri, R. A., Barnard, J. C., Easter, R. C., Riemer, N., and West, M.: Particle-resolved simulation of aerosol size, composition, mixing state, and the associated optical and cloud condensation nuclei activation properties in an evolving urban plume, Journal of Geophysical Research: Atmospheres, 115, https://doi.org/10.1029/2009JD013616, 2010.

Zaveri, R. A., Wang, J., Fan, J., Zhang, Y., Shilling, J. E., Zelenyuk, A., Mei, F., Newsom, R., Pekour, M., Tomlinson, J., Comstock, J. M., Shrivastava, M., Fortner, E., Machado, L. A. T., Artaxo, P., and Martin, S. T.: Rapid growth of anthropogenic organic nanoparticles greatly alters cloud life cycle in the Amazon rainforest, Science Advances, 8, eabj0329, 10.1126/sciadv.abj0329, 2022.

Zhang, H., Kondragunta, S., and Ciren, P.: TEMPO Aerosol Optical Depth and Aerosol Layer Height Retrieval Algorithm, Journal of Geophysical Research: Atmospheres, 130, e2025JD044082, https://doi.org/10.1029/2025JD044082, 2025.

Zhang, Q., Jimenez, J. L., Canagaratna, M. R., Allan, J. D., Coe, H., Ulbrich, I., Alfarra, M. R., Takami, A., Middlebrook, A. M., Sun, Y. L., Dzepina, K., Dunlea, E., Docherty, K., DeCarlo, P. F., Salcedo, D., Onasch, T., Jayne, J. T., Miyoshi, T., Shimono, A., Hatakeyama, S., Takegawa, N., Kondo, Y., Schneider, J., Drewnick, F., Borrmann, S., Weimer, S., Demerjian, K., Williams, P., Bower, K., Bahreini, R., Cottrell, L., Griffin, R. J., Rautiainen, J., Sun, J. Y., Zhang, Y. M., and Worsnop, D. R.: Ubiquity and dominance of oxygenated species in organic aerosols in anthropogenically-influenced Northern Hemisphere midlatitudes, Geophysical Research Letters, 34, https://doi.org/10.1029/2007GL029979, 2007.

Zhang, Q. J., Beekmann, M., Freney, E., Sellegri, K., Pichon, J. M., Schwarzenboeck, A., Colomb, A., Bourrianne, T., Michoud, V., and Borbon, A.: Formation of secondary organic aerosol in the Paris pollution plume and its impact on surrounding regions, Atmos. Chem. Phys., 15, 13973–13992, 10.5194/acp-15-13973-2015, 2015.